A geometric and deep learning reproducible pipeline for monitoring floating anthropogenic debris in urban rivers using in situ cameras

Gauthier Grimmer^a, Romain Wenger^{a,*}, Clément Flint^{b,c}, Germain Forestier^{d,e}, Gilles Rixhon^a, Valentin Chardon^a

^aLIVE UMR 7362 CNRS, University of Strasbourg, 3 rue de l'Argonne, Strasbourg, 67000, France

^bCentre Inria de l'Université de Lorraine, 615 rue du Jardin

Botanique, Villers-lès-Nancy, 54600, France

^cTechnical University of Munich, Campus Heilbronn, Bildungscampus

2, Heilbronn, 74076, Germany

^dIRIMAS UR 7499, University of Haute-Alsace, 12 rue des Frères

Lumière, Mulhouse, 68000, France

^eData Science and Artificial Intelligence (DSAI), Monash

University, Melbourne, Australia

Abstract

The proliferation of floating anthropogenic debris in rivers has emerged as a pressing environmental concern, exerting a detrimental influence on biodiversity, water quality, and human activities such as navigation and recreation. The present study proposes a novel methodological framework for the monitoring the aforementioned waste, utilising fixed, in-situ cameras. This study provides two key contributions: (i) the continuous quantification and monitoring of floating debris using deep learning and (ii) the identification of the most suitable deep learning model in terms of accuracy and inference speed under complex environmental conditions. These models are tested in a range of environmental conditions and learning configurations, including experiments on biases related to data leakage. Furthermore, a geometric model is implemented to estimate the actual size of detected objects from a 2D image. This model takes advantage of both intrinsic and extrinsic characteristics of the camera. The findings of this study underscore the significance of the

^{*}Corresponding author. Email address: romain.wenger@live-cnrs.unistra.fr (R.Wenger)

dataset constitution protocol, particularly with respect to the integration of negative images and the consideration of temporal leakage. In conclusion, the feasibility of metric object estimation using projective geometry coupled with regression corrections is demonstrated. This approach paves the way for the development of robust, low-cost, automated monitoring systems for urban aquatic environments.

Keywords: Waterways management, Deep Learning, In Situ Camera, Open Data, Remote Sensing

1. Introduction

Several million tonnes (1.15–2.41 Mt) of anthropogenic debris are transported annually to the oceans via hydrosystems (Lebreton et al., 2017; González-Fernández et al., 2021; Palmas et al., 2022). Their presence in rivers results from both anthropogenic activities—such as poor waste management, illegal dumping, waste-water treatment or urbanisation (Van Emmerik and Schwarz, 2020; Schöneich-Argent et al., 2020; De Vries et al., 2021)—and natural processes like aerial deflation and rainfall induced surface runoff (Van Emmerik and Schwarz, 2020). This accumulation can be particularly significant downstream of urban areas, due to high population density and socio-economic activities significantly contribute to various debris inputs into hydrosystems (Rech et al., 2014; Van Emmerik and Schwarz, 2020; Gómez et al., 2022). Anthropogenic debris—including plastics, metals, and glass (Hanke et al., 2013; Suteja et al., 2025)—represent a major environmental concern, especially in the context of urban river management. Plastics alone accounts for approximately 80% of these debris (Rech et al., 2014; González-Fernández et al., 2021), making it a pervasive pollutant affecting all ecosystems.

In rivers, macroplastics (> 5 mm; González-Fernández et al., 2021) degrade into microplastics (< 5 mm; Skalska et al., 2020) through biochemical (i.e. photodegradation, oxidation, biodegradation) and mechanical (i.e. movement of water and sediment, etc.) fragmentation (Liro et al., 2023). Aligned with the One Health approach (Prata et al., 2021; Bois and Staentzel, 2025), macroplastics harm wildlife (i.e. entanglement, intestinal blockage; Waring et al., 2018; Alabi et al., 2019) and promote bank overflow and flooding eventually resulting in river morphology alterations (Van Emmerik and Schwarz, 2020). The average concentration of 6.7 particles of microplastics

per cubic metre of water (Ghiglione et al., 2023; Landebrit et al., 2024) represents a growing environmental and public health concern. Furthermore, microplastics interfere with natural ecosystem functions (i.e. nutrient flow, species reproduction, etc.; Prata et al., 2021) and are easily found in the trophic chain through the consumption of fish (Neves et al., 2015) or other products containing plastics (Kumar et al., 2022). Plastics directly impact health due to additives like Bisphenol A and Persistent Organic Pollutants (POPs), associated with neurological and reproductive issues (Alabi et al., 2019). This underlines the need to monitor riverine debris to reduce macroand microplastics input in hydrosystems.

Riverine anthropogenic debris and their spatial dynamics have been studied so far through direct monitoring methods. The latter include: (i) GPS (Tramoy et al., 2019) or RFID trackers (Chardon et al., 2025), (ii) debris quantification via visual observation (Castro-Jiménez et al., 2019), (iii) net sampling from bridges or boats (Hurley et al., 2023), or (iv) passing sampling (i.e. use of existing infrastructure; Van Emmerik and Schwarz, 2020). Although these methods are efficient at the local scale, they fail, at the catchment scale, to continuously monitor debris flux and capture anthropogenic debris heterogeneity (Hurley et al., 2023). These inherent limitations call for new automated approaches enabling continuous monitoring and the production of reproducible results.

In this respect, camera-acquired digital images has been recently used to tackles issues related to anthropogenic debris (Van Lieshout et al., 2020; Donal et al., 2023; Zhang et al., 2023) because they allow continuous recording and thereby capturing data variability (i.e. debris diversity, water turbidity, weather conditions; Jia et al., 2023; Tata et al., 2021). In connection with riverine debris monitoring, deep learning (DL) methods are inscreasingly widespread. Van Lieshout et al. (2020) and Kataoka et al. (2024) used cameras mounted on bridges characterised by vertical views. Maharjan et al. (2022) use cameras onboard UAVs. Images captured by these methods are then processed with convolutional neural networks (CNNs)—such as Faster R-CNN (Van Lieshout et al., 2020), YOLOv5-s (Armitage et al., 2022) or YOLOv8 (Kataoka et al., 2024)—achieving high detection performance on riverine debris. However, both approaches are either intrisically linked to a fixed spot (i.e. cameras on bridges) or limited in time (i.e. punctual monitoring by cameras mounted on UAVs).

On the one hand, becoming independent of man-made structures is thus a prerequisite when it comes to study anthropogenic debris fluxes at the catchment scale. On the other hand, the flexible implementation of cameras along streams results in issues related to heterogeneous observation conditions which can accentuate biases and negatively impact the robustness of DL models. This study thus first seeks to examine the object detection capacity of CNN models in complex recording conditions that are river environments. The second challenge after debris detection is to estimate its dimensions, taking into account the geometric distortions in the image caused by the environment hosting the cameras.

The threefold aims of this study are: (i) continuous quantification and monitoring of floating debris using DL models, (ii) identifying the most suitable DL model in terms of accuracy and inference speed under complex environmental conditions, and (iii) proposing a generalisable solution by introducing a geometric modeling approach to the camera's field of view in order to estimate the dimensions of real-world objects from image-based detections.

2. Methodology

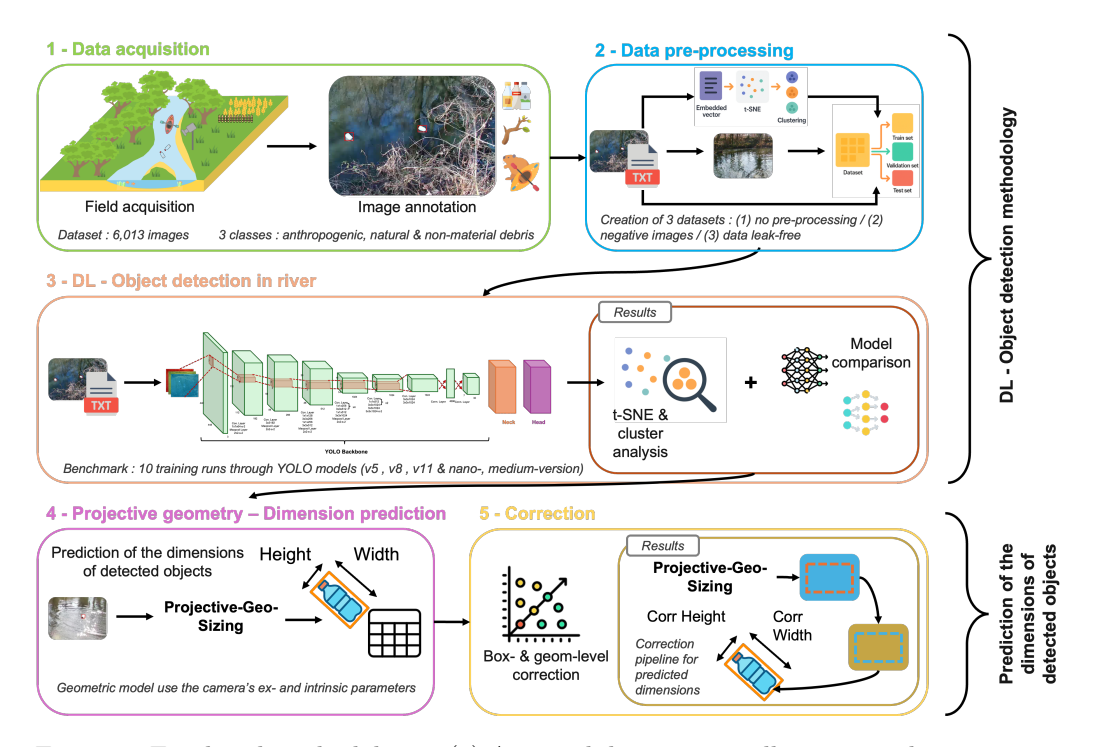


Figure 1: Employed methodology: (1) Acquired data is manually annotated to constitute initial dataset. (2) The latter is pre-processed so that (3) several models can then be trained to detect debris in rivers. (4) Dimensions of detected objects are predicted and then (5) corrected to reduce errors

2.1. Study area

The natural reserve of the *Robertsau* and *Wantzenau* forest massif is located north of the Greater Strasbourg (Fig.2). A protected natural zone was established in 2020, and covers an area of 710 hectares in total. Its biodiversity encompassing a variety of natural environments, including deciduous forests, waterways, arable lands, and wetlands makes it peculiar. The forest massif of the reserve is considered representative of alluvial environments. Although the Rhine River has now been dammed up, it still exerts a significant influence, notably through groundwater level changes. This diversity of habitats supports a wide variety of flora and fauna, including species such as the European beaver, the European eel, the elm or the superb carnation (Réserves Naturelles de France, 2023).

The Steingiessen river flows through this nature reserve (Fig.2). This sinuous watercourse is 4.5 kilometers long. It is part of the Greater Strasbourg hydrographic system as a defluent of the Ill river, which flows further downstream into the Rhine drainage canal. The latter, via the Ill diversion canal, joins the Rhine River downstream of the Gambsheim hydroelectric dam.

2.2. Data

2.2.1. In situ data collection

For this study, two pan-tilt-zoom (PTZ) cameras were used to capture model training data. These cameras were positioned upstream and downstream of the Steingiessen River (Fig. 2). Anthropogenic debris and wood were manually inserted into the river. On March 4, 2025, between 10 and 12 a.m, anthropogenic debris (glass bottles, plastic bags, polystyrene, plastic bottles) and wood were manually added upstream of the first camera. At the same time, kayak passages were made. The same protocol was repeated from 3 to 4 p.m. on the downstream camera. The final dataset contains a total of 6,013 images.



Figure 2: Location of Steingiessen River and inlet and outlet cameras (north of Greater Strasbourg)

2.2.2. Image labelling and ground truth data creation

The first step in object detection is data labelling (Fig.1). The images are manually annotated using the *LabelImg* tool (Tzutalin, 2015), with the annotation process consisting of the creation of bounding boxes around objects (Fig.3) (Aarnink et al., 2025). The annotation process was made according to following typology: (1) anthropogenic debris, (2) natural debris, and (3) non-debris material (floating boats). The initial dataset contains: 10,873 anthropogenic debris, 754 natural debris, and 1,010 non-debris materials.





Figure 3: Data acquired on March 4, 2025 upstream (left) and downstream (right) of the Steingiessen River. Bounding boxes on anthropogenic debris and non-debris materials. Bounding boxes have been manually digitized.

2.2.3. Negative images acquisition

The incorporation of negative images, which are images with no objects, is intended to respond to the reduction in bias hypothesis (Malagon-Borja and Fuentes, 2009). Indeed, the presence of objects on the river surface can be overestimated due to variable recording conditions (luminosity, reflections, and eddies).

Negative images were selected for the month of February 2025. Variables relating to sunshine were used to select days of either sunny or cloudy weather conditions. They are: (1) Daily insolution duration (INST); (2) Daily global irradiance (GLOT); (3) and fraction of sunshine in relation to day length (SIGMA). The variables were normalised to determine the days of interest (Fig.4). Consequently, 10 February 2025 was identified as a day characterised by low levels of sunshine, while 20 February 2025 was considered a day with clear skies. In addition, negative images were acquired from the upstream and downstream cameras.

A total of 14,030 negative images were acquired: 7,098 and 6,932 images were recorded on 10 and 20 February, respectively (Fig.4).

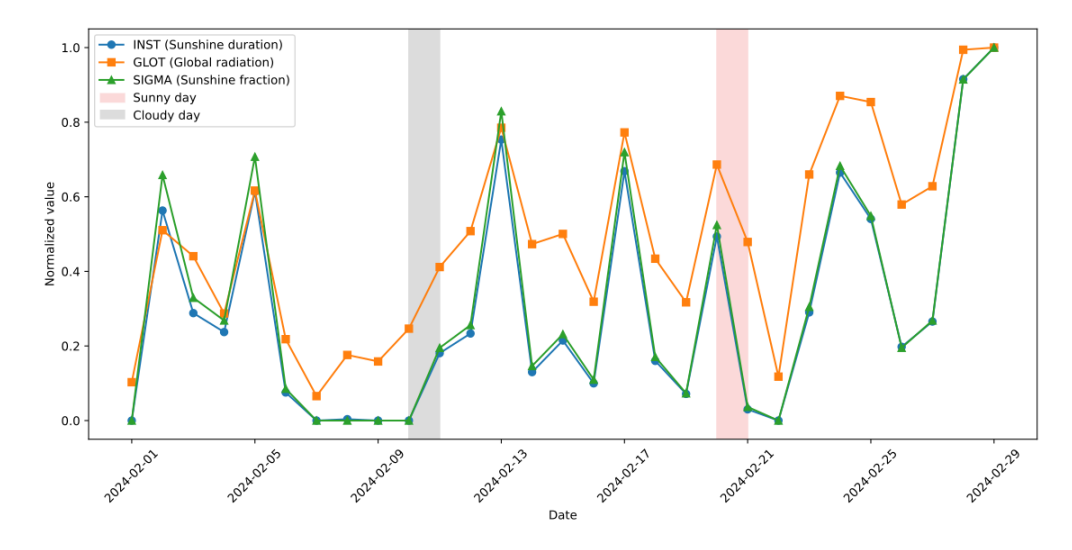


Figure 4: Evolution of Daily Insolation Duration (INST), Daily Global Radiation (GLOT) and fraction of sunshine in relation to day length (SIGMA) during February 2025 at the Strasbourg - Entzheim weather station (France) ("Données climatologiques de base quotidiennes", Météo-France, 2025). In grey, cloudy weather and in pink, sunny weather.

2.3. Data leakage

Splitting image data into three subsets (train, validation, test) can lead to data leakage. This occurs when a subset of the training data is also used in the test data (Babu et al., 2024). The data leakage problem can distort the actual performance of the object detection model by overestimating or underestimating performance measures (Babu et al., 2024). This error can occur itself in various ways, notably in features and temporal data (John et al., 2025). In our case, the use of data in unvaried forms (i.e. the majority of anthropogenic debris are plastic bottles) and temporal data can lead to data leakage. To limit this phenomenon, we assemble image data into groups that contain images with the same temporal scene and, therefore, the same debris.

2.3.1. Images features extraction

There is a lot of redundant information in image data, and in order to group it together, it is necessary to reduce their dimensionality representation by extracting features (Figueiredo and Mendes, 2024). As a first step, a pretrained YOLOv8 (You Only Look Once) model was used to extract visual

features from images in its 21st back layer (Fig.5). This generates a 256-length embedded vector. This means that the 21st layer of the YOLOv8 encoder has identified 256 visual features in each image. In addition, we extracted features from the labelling annotation for each image, such as the number of objects per class and information about the bounding box of the annotated objects. The timestamps were extracted and added to the final vector, creating an embedded vector for 6,013 images, 261 in length. Given the size of the data, it is necessary to reduce it to two dimensions for better analysis.

2.3.2. Dimension reduction using t-Distributed Stochastic Neighbor Embedding

t-SNE (t-Distributed Stochastic Neighbor Embedding) is a non-linear, unsupervised method to map data into reduced dimensions (generally 2 dimensions) (Anowar et al., 2021) while preserving the significant structure of the original data (Figueiredo and Mendes, 2024). It reduces dimensionality by converting the Euclidian distance between high-dimensional data points into conditional probabilities representing similarities (Oliveira et al., 2018), calculated as:

$$p_{a|b} = \frac{\exp\left(-\frac{\|x_b - x_a\|^2}{2\sigma^2}\right)}{\sum_{a \neq k} \exp\left(-\frac{\|x_k - x_a\|^2}{2\sigma^2}\right)}$$
(1)

where x_a and x_b are two data points. It calculates how close is x_a is from x_b considering a Gaussian distribution around x_b with a given variance σ^2 (Anowar et al., 2021). When the probabilities of distributions are calculated, the aim is to minimize the difference between two points. The function to be minimized is the sum of the Kullback-Leibler divergences at all points with a gradient descent (Oliveira et al., 2018):

$$E = \sum_{a} KL(P_a \parallel Q_a) = \sum_{a} \sum_{b} p_{b|a} \log \frac{p_{b|a}}{q_{b|a}},$$
 (2)

where P_a represents the conditional probability distribution measuring the similarity between the point x_a and all other data points in the original space, while Q_a is the corresponding conditional probability distribution computed from the projected point y_a in the low-dimensional space (Oliveira et al., 2018). Therefore, t-SNE was calculated with a perplexity of 30 and a learning rate of 200.

2.3.3. DBSCAN clustering

Clustering groups similar data based on clear, meaningful similarity and dissimilarity measures, aiming for high intra-group similarity and a strong inter-group difference (Wegmann et al., 2021). After dimensionality reduction, clustering is used to group images from the same scene. Density-based Spatial Clustering of Application with Noise (DBSCAN) algorithm was chosen to cluster images (Figueiredo and Mendes, 2024). This density-based algorithm detects clusters as high-density area that can grow in any direction, allowing the identification of arbitrary-shaped groups, outliers, and noise. (Wegmann et al., 2021). DBSCAN was applied with an eps of 5 and a minimum sample of 10.

2.3.4. Clustering validation

The clustering performance was assessed using the DBCV (Density-Based Clustering Validation) index. This metric combines local density with structural separation to evaluate cluster quality. Initially, the core distance for each point is calculated, representing the inverse of its local density. Subsequently, a minimum spanning tree is employed to capture the internal structure for each cluster. The subsequent extraction of density sparseness and density separation is achieved through this process. Then these components are used to compute a metric that evaluates how dense and well-separated the clusters are (Wegmann et al., 2021). DBCV is calculated as:

$$DBCV(C) = \sum_{i=1}^{l} \frac{|C_i|}{|O|} \cdot V_C(C_i)$$
(3)

where C is the set of all clusters, l is the total number of clusters, $|C_i|$ is the number of points in cluster C_i , |O| is the total number of data points, and $V_C(C_i)$ is the local validity score of cluster C_i , based on its internal density and its separation from other clusters (Moulavi et al., 2014).

2.4. Dataset creation

Three datasets were created. The first one has been created by a random split of 80% for the training set, 10% for the validation set, and 10% for the

testing set. It contains 6,013 images for a total of 12,637 objects of all classes. The training set contains 8,635 anthropogenic debris, 601 natural debris, and 824 non-debris material. The validation set contains 1119 anthropogenic debris, 76 natural debris ,and 105 non-debris material. Finally, the testing set contains 1119 anthropogenic debris, 77 natural debris and 81 non-debris material.

The second set of data comprises the first set, plus an additional 30% of negative images. As a result, there is 2,064 negative images in the training set, 259 in the validation set and 257 in the test set.

The third dataset was created using a random split (80/10/10) on clusters created by DBSCAN clustering after dimension reduction using t-SNE. Each cluster is randomly placed in one of the three sets (training, validation and testing) to avoid separation. Thus, the training set contains 8,978 anthropogenic debris, 424 natural debris and 465 non-debris material. The validation set contains 475 anthropogenic debris, 145 natural debris, and 330 non-debris material. Finally, the testing set contains, 1,198 anthropogenic debris, 185 natural debris, and 215 non-debris material.

2.5. Deep learning approach

2.5.1. Selecting Convolutional Neural Network

Convolutional neural networks (CNNs) are algorithms dedicated to processing data in the form of multiple matrices, such as signals and sequences, images, or videos. CNNs are composed of a cascading sequence of convolution and pooling layers, which extract essential features from the input data to perform class prediction (LeCun et al., 2015). The convolution layer extracts the main features of data such as textures or edges by applying a convolutional kernel on it. In addition, the pooling layer performs a sampling action on the feature maps derived from the convolution layers to reduce their spatial dimensionality (Schwindt et al., 2024) (Fig. 5).

In the context of object detection methodologies, several CNN architectures are used, such as the R-CNN (Van Lieshout et al., 2020) or You Only Look Once (YOLO) algorithm (Aarnink et al., 2025). R-CNN algorithms are based on a region-of-interest method. First, they generate potential bounding boxes and classify them. The algorithm then performs a long-time post-processing (Aarnink et al., 2025), including removing detections and correcting bounding boxes by analysing other detections in the image (Girshick et al., 2014). In contrast, the YOLO model processes the entire image during the detection phase (Redmon et al., 2016). Due to this,

the processing time of the YOLO algorithm is shorter, while its performance appears higher (Aarnink et al., 2025; Redmon et al., 2016). Consequently, the YOLO algorithm was selected for this study.

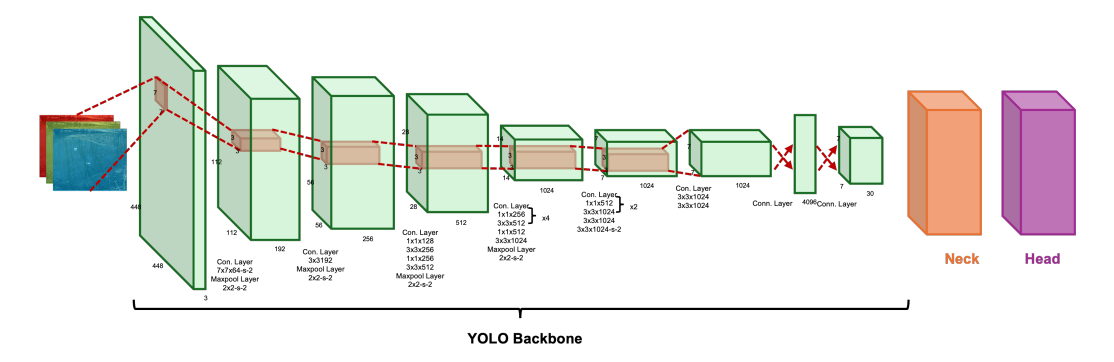


Figure 5: General architecture of a YOLO object detection model. The structure is divided into three main components: the **backbone**, responsible for extracting hierarchical features from the input image using a series of convolutional and pooling layers; the **neck**, which enhances feature aggregation across different scales (often using modules such as PANet or FPN in recent versions); and the **head**, which performs final object detection by predicting bounding boxes, objectness scores, and class probabilities. While the figure reflects a simplified backbone resembling early YOLO versions, the general structure remains consistent across modern versions such as YOLOv5, YOLOv8, and YOLOv11, with architectural refinements aimed at improving speed and accuracy.

2.5.2. Implementation details

Data augmentation was performed (De Vries et al., 2021). The data augmentation parameters are as follows; vertical tilting on 50% of images, horizontal tilting on 50% of images, activation of mosaic augmentation, hue variation (0.015), saturation variation (0.7), brightness variation (0.4), perspective distortion (0.0005), random resizing on 50% of images and random transition. Above all, this increases the amount of input data to the model (Kylili et al., 2019), but also adds variability to the dataset and increases its robustness (Aarnink et al., 2025).

The number of epochs is set to 200. All calculations were performed with an Nvidia GeForce GTX 1080ti graphics processing unit (GPU) with 11GB of VRAM. The training scenarios (see section 2.5.3) include YOLO nano and medium models. Being limited in computing power, the nano models were run with a batch size of 32, while the medium variants of the models were run with a batch size of 8. In addition, the image size is fixed at 1280 pixels. This patch size enables the model to improve the detection of smaller objects

and avoid misclassification due to lighting differences. To optimize training, the learning rate (LR) was set at 0.001. To limit LR descent, a final learning rate (FLR) is set at 0.2, in conjunction with cosine annealing (Ultralytics Inc., 2019). A LR planner adjusts the LR according to a cosine curve, thus limiting the risk of exceeding the optimal LR value (Schwindt et al., 2024). Finally, a momentum (0.937) is introduced to facilitate the incorporation of previous gradients into new epochs (Ultralytics Inc., 2019).

One of the recurrent challenges encountered during the training of DL algorithms pertains to the issue of overfitting. This occurs when the model performs very well on the training dataset but has great difficulty generalizing to the test dataset (Ying, 2019). To limit this effect, an early-stopping callback, with a patience of 10 epochs, has been integrated into the hyperparameters of the trained models. This approach serves to mitigate the impact of noise learning on the model's accuracy. So, if model accuracy falls continuously over 10 epochs, early-stopping stops learning and retains the best epoch of training. In addition, an L2 (0.0005) regularization has been applied, notably to limit the weights of features with little significance in model learning (Ying, 2019).

2.5.3. Experimental design for YOLO-based object detection

Training was performed using transfer learning (Donal et al., 2023). This method involves using artificial neural network models pre-trained on other datasets. The architecture, weights, and biases of the models are then used to train the new model (Schwindt et al., 2024). Three variants of the YOLO algorithms were tested: YOLOv5, YOLOv8 and YOLOv11. These algorithms, dedicated to object detection, are models pre-trained on the COCO dataset (Lin et al., 2014) proposed by Microsoft, which contains 80 object classes. To determine the best-performing model for multiclass object detection in watercourses, 10 scenarios were tested:

- YOLOv5-n (yolov5n): the YOLOv5-n model is trained on the initial dataset, with the hyperparameters described above.
- YOLOv5-m (yolov5m): the YOLOv5-m model is trained on the initial dataset with the hyperparameters previously set.
- YOLOv8-n (yolov8n): the YOLOv8-n model is trained on the initial dataset with the hyperparameters previously set.

- YOLOv8-m (yolov8m): the YOLOv8-m model is trained on the initial dataset with the hyperparameters previously set.
- YOLOv11-n (yolov11n): the YOLOv11-n model is trained on the initial dataset with the hyperparameters previously set.
- YOLOv11-m (yolov11m): the YOLOv11-m model is trained on the initial dataset with the hyperparameters previously set.
- YOLOv8-n with negative images (yolov8n-neg30): the YOLOv8-n model is trained on a new dataset consisting of the first dataset (not the one based on clustering method) and negative images. In this case, negative images represent 30% of the total dataset. In the testing set, 256 negative images were introduced, of which 128 images corresponded to the sunny day and 128 to the cloudy day. In the training set, 2,063 negative images were added, of which 1,031 were for the sunny day and 1,032 for the cloudy day. Finally, in the validation set, 258 negative images were added, including 129 sunny day and 129 cloudy day images.
- YOLOv11-m with negative images (yolov11m-neg30): the YOLOv11-m model is trained on the same dataset as the yolov8n-neg30 scenario, i.e. the dataset consisting of 30% negative images.
- YOLOv8-n-cluster: the YOLOv8-n model is trained on the second dataset, created by random split on clusters. It is trained with hyperparameters previously set.
- YOLOv11-m-cluster: the YOLOv11-m model is trained on the second dataset, created by random split on clusters. It is trained with hyperparameters previously set.

2.5.4. Model evaluation

Indices such as precision, recall, mAP@50, and mAP@50-95 are used to assess the performances of the different models. To obtain these indices, the models are applied to the test sets. Recall (Eq. 4) represents the proportion of objects detected among all the objects present in the image. Precision (Eq. 5) indicates the proportion of all detected objects that are actually detected. The mAP (mean Average Precision) corresponds to a measure of object detection performance based on an IoU (Intersection over Union) between the predicted bounding box and that of the reference data (Maharjan

et al., 2022). To this end, the mAP_{@50} (Eq. 6) uses a 50% IoU threshold to check whether the detected objects overlap at least 50% with the real object detected manually. The $mAP_{[.50:.95]}$ (Eq. 7) uses a more precise IoU (Eq. 8) threshold and performs an average accuracy at each overlap threshold over a threshold step of 0.05. Recall, Precision, mAP_{@50}, $mAP_{[.50:.95]}$ and IoU can be defined as follows

$$Recall = \frac{True \ Positives}{True \ Positives + False \ Negatives}$$
 (4)

$$Precision = \frac{True \ Positives}{True \ Positives + False \ Positives}$$
 (5)

$$mAP_{@50} = \frac{1}{N} \sum_{i=1}^{N} AP_i^{IoU=0.50}$$
(6)

where N is the number of classes, AP_i is the average precision for class i.

$$\text{mAP}_{[.50:.95]} = \frac{1}{10} \sum_{k=0}^{9} \left(\frac{1}{N} \sum_{i=1}^{N} \text{AP}_{i}^{\text{IoU}=0.50+0.05k} \right)$$
 (7)

where $AP_i^{IoU=t}$ is the AP for class i at IoU threshold t, t in $\{0.50, 0.55, \dots, 0.95\}$, N is the number of classes.

$$IoU = \frac{|B_{pred} \cap B_{gt}|}{|B_{pred} \cup B_{gt}|}$$
(8)

where B_{pred} is the predicted bounding box and B_{gt} is the ground truth bounding box.

Alongside these performance metrics, indices related to model processing time were measured. For each model, the inference time as well as the number of images processed per second on CPU were taken into account (Tata et al., 2021).

2.6. Object size estimation by geometric model

We used tools from projective geometry (Birchfield, 1998) to extrapolate object dimensions from the bounding boxes provided by the YOLO models. Estimating real-world sizes from 2D detections requires converting pixel coordinates into 3D features, such as lengths, coordinates, directions, etc. For this, assumptions about the mapping must be made. We adopt the pinhole

camera model, which treats each pixel as corresponding to a ray passing through the camera's optical center. This provides a simplified yet effective approximation of the image formation process, ignoring lens distortion and treating the projection as perfectly linear.

We explicitly reconstruct these rays using known intrinsic camera parameters (focal length, sensor size) and extrinsic installation data (camera height and angle), rather than relying on matrix-based projective transformations. The rays are then intersected with a reference ground plane to recover metric object dimensions, such as width and height, from the projected bounding box edges.

Our framework does not account for real-world optical artifacts such as lens distortion, remaining strictly within the assumptions of the ideal pinhole camera model. In section 2.7, we evaluate the accuracy of our approach by comparing its predicted object dimensions against manually measured ground truth. While more advanced lens correction techniques exist, they were deemed unnecessary in our context due to the acceptable level of accuracy achieved; however, they could be integrated into the model in future work to further reduce systematic errors (Mohr and Triggs, 1996).

We treat each pixel as a ray that originates at the camera's optical center and passes through the corresponding point on the image sensor, to determine the 3D orientation of a given pixel in the image,

The first step is to compute the effective focal lengths along the horizontal and vertical axes, denoted f_x and f_y , expressed in *pixels*. These values indicate how many pixels correspond to the camera's optical focal length in each direction:

$$f_x = \frac{W \cdot f}{w_s} \tag{9}$$

$$f_y = \frac{H \cdot f}{h_s} \tag{10}$$

Here, f is the optical focal length of the camera, in millimeters; w_s and h_s are the physical width and height of the sensor, also in millimeters; W and H are the image width and height in pixels. The resulting f_x and f_y represent the focal length in pixels, i.e., the number of pixels that correspond to one focal length unit along each axis.

Thanks to the focal length, we can reason in pixel coordinates within the

image (Figure 6c). With f_x , f_y , and the image center (c_x, c_y) defined as:

$$c_x = \frac{W-1}{2}, \quad c_y = \frac{H-1}{2},$$

we compute the local ray direction associated with any pixel (x_{pix}, y_{pix}) using the following formula:

$$\vec{v}_{\text{local}} = \text{normalize} \left(\begin{bmatrix} (x_{\text{pix}} - c_x)/f_x \\ (c_y - y_{\text{pix}})/f_y \\ -1 \end{bmatrix} \right)$$
 (11)

This vector is expressed in the camera's local coordinate system, where the optical axis is aligned with the negative z-axis. The horizontal and vertical terms map the pixel's displacement from the image center (c_x, c_y) , scaled by the respective focal lengths f_x and f_y , so that they correspond to physical angular offsets. Here, the y coordinates are flipped to match the standard computer vision convention, where the top of the image corresponds to positive y in pixel space but to negative y in the 3D camera frame. These expressions effectively project the focal cone onto a virtual image plane placed at z = -1: a pixel exactly at the center maps to the direction (0, 0, -1), while other pixels yield rays tilted accordingly. The normalize operation ensures the resulting vector is a unit-length direction vector.

Finally, the local ray is rotated according to the camera's orientation. In general, a camera's orientation is described by three successive rotations: a pitch angle ϕ (rotation around the horizontal x-axis), a yaw angle θ (rotation around the vertical y-axis), and a roll angle (rotation around the optical z-axis). Each of these affects the perceived direction of rays in different ways.

In our setup, only the pitch angle ϕ , which controls the vertical inclination of the camera, is taken into account. The yaw angle θ is ignored, as it rotates the camera parallel to the ground and does not affect object size estimation. The roll angle remains zero throughout the acquisition, as the camera stays horizontally aligned.

We can, therefore, define a rotation matrix as

$$R_x(\phi) = \begin{bmatrix} 1 & 0 & 0 \\ 0 & \cos \phi & -\sin \phi \\ 0 & \sin \phi & \cos \phi \end{bmatrix}$$
 (12)

and compute the the ray direction in actual world coordinates:

$$\vec{v}_{\text{world}} = R_x(\phi) \cdot \vec{v}_{\text{local}},$$
 (13)

where \vec{v}_{local} is the pixel direction computed from equation 11.

This mapping from image pixels to 3D rays forms the geometric backbone of our estimation process: from these rays, we construct planes, compute intersections, and measure distances to recover metric dimensions. For conciseness, we omit the derivation of these standard geometric operations (plane construction, ray-plane intersections, point-to-plane distances); they are recapped in the appendix for reference.

We compute five directional vectors of interest: $\vec{v}_{\text{top-left}}$, $\vec{v}_{\text{top-right}}$, $\vec{v}_{\text{bottom-left}}$, $\vec{v}_{\text{bottom-right}}$, and \vec{v}_{center} . Each vector corresponds to a key point of the bounding box: its four corners and its center. This process is schematized in Figure 6d. They indicate the direction in world space along which that point is observed from the camera.

From the four corner vectors, we construct four planes by pairing each adjacent corner with the camera's optical center, denoted as \vec{C} . For example, the top edge of the bounding box defines the plane:

$$\Pi_{\text{top}} = \text{Plane}(\vec{C}, \vec{v}_{\text{top-left}}, \vec{v}_{\text{top-right}}),$$

and similarly for the bottom, left, and right edges. These planes form a pyramid-like volume spanning from \vec{C} that encloses the region in space where the object is assumed to lie.

Since the object's distance from the camera is not known *a priori*, we estimate its position by intersecting the central ray \vec{v}_{center} with the ground plane (Fig. 6e). This intersection yields a single 3D point, denoted as \vec{O} that we take as a proxy for the object's center location in space.

The object's width and height are then estimated by summing the distances from \vec{O} to the pairs of vertical and horizontal bounding planes:

$$dim_x = \operatorname{distance}(\vec{O}, \Pi_{\text{left}}) + \operatorname{distance}(\vec{O}, \Pi_{\text{right}})$$
 (14)

$$dim_y = \operatorname{distance}(\vec{O}, \Pi_{\text{top}}) + \operatorname{distance}(\vec{O}, \Pi_{\text{bottom}}).$$
 (15)

Figure 6f shows a visual interpretation of these distances from the camera's perspective.

This geometric pipeline provides a fully interpretable method for estimating the object dimensions dim_x and dim_y from monocular images. However, due to real-world deviations from the ideal pinhole model—such as lens distortion, imperfect camera alignment, wrong bounding box positioning, and ground unevenness—we observe slight discrepancies between predicted and actual object sizes. In the next section, we describe how an a posteriori correction is applied to compensate for these systematic biases and improve the accuracy of our estimates. Formulas are detailed in the Appendix A.

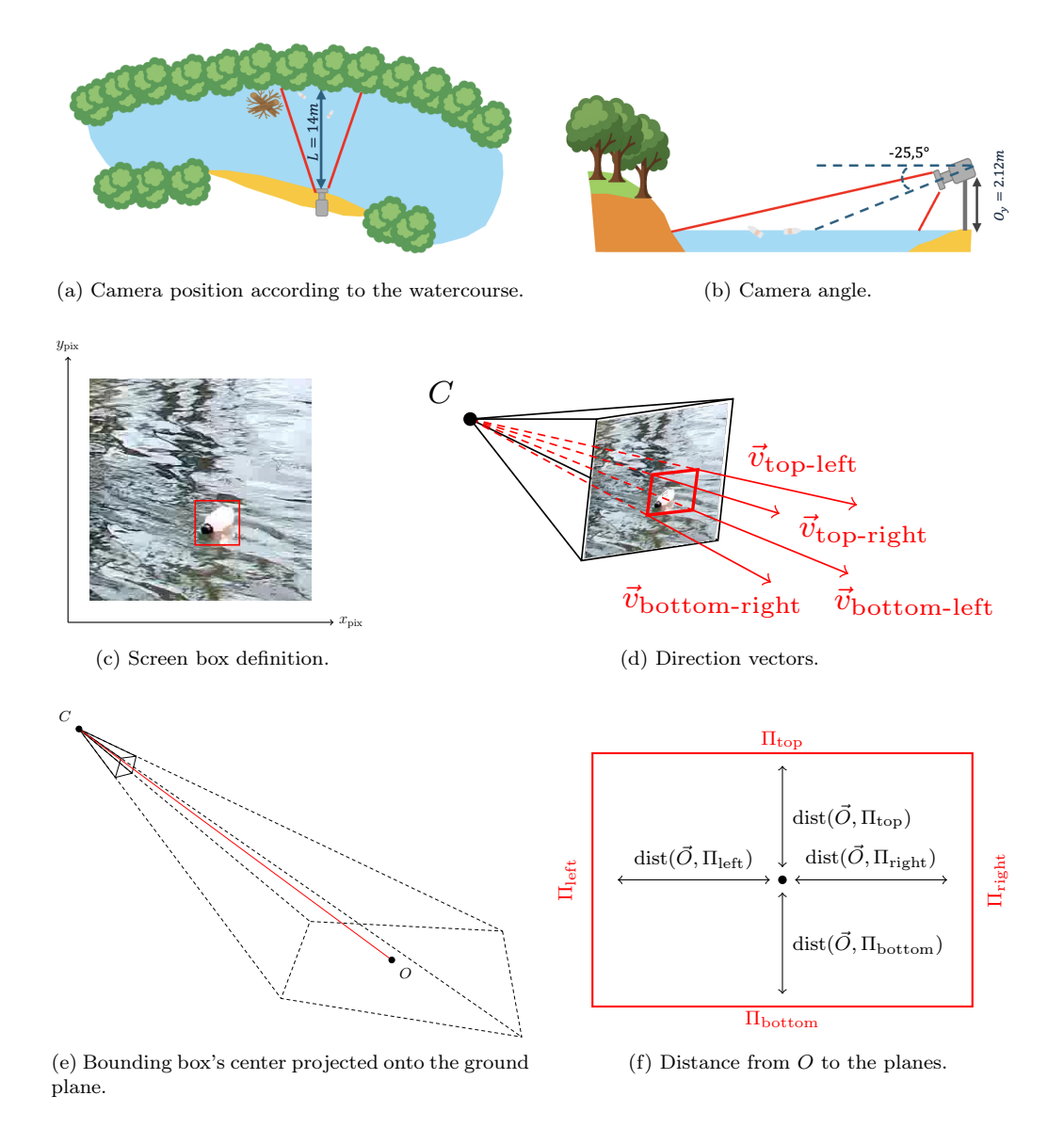


Figure 6: Visualization of the object size estimation process. Subfigures 6a and 6b illustrate the camera's field of view setup. Subfigure 6c shows the bounding box in 2D. Subfigure 6d illustrates how this box is lifted into 3D space via ray projections from the camera center. Subfigure 6e depicts the intersection of these rays with the ground plane, forming a spatial footprint of the object. Finally, Subfigure 6f shows the 4 distances from the camera's perspective.

2.7. Metrics and size of detected bounding box correction

A pipeline of two corrections was applied to the dimensions predicted by the geometric model on the bounding boxes predicted by the object detection model.

The first correction (Bounding box shape correction) corrects the shapes of the bounding boxes predicted by the AI model. This correction uses the predicted dimensions of the bounding boxes detected by the AI model as the data to be corrected. The reference data corresponds to the dimensions predicted on the manually annotated bounding boxes (Fig.7). Here, the aim is to correct systematic biases in the estimated physical dimensions of detected objects, caused by imperfect alignment between the annotated bounding boxes and the actual physical extents of the objects. It is important to note that this correction is applied solely in the physical space, without relying on the bounding box coordinates themselves.

The second correction (Predicted dimensions correction) aims to correct the dimensions (width and length) predicted by the geometric model on the corrected shape of the bounding boxes (Fig.7). Here, the reference data is created by manually measuring the dimensions of the objects. With this correction, we are looking to refine the predicted dimensions.

As a result, we expect each individual correction to improve the precision of the method. We will also look at the relevance of combining the two corrections

Correction pipeline Predicted data 2 - Box shape correction data Height Projective-Geo-Reference Sizing Annoted bounding box Shape reference data : created by manually annotated bounding box (Labellmg) Predicted Shape correction: predicted dimensions are bounding box corrected according to box reference data Shape-level corrected dimensions -Box dimension correction Projective-Geo-Height Width data Results Sizing Reference Error reduction Manually measured Predicted Dim. reference data: manually measured dimensions in laboratory condition Corr height Dim.-level Dim correction : Box-level dimensions are The AI model detect object and geometric corrected corrected according to geom reference model predict its dimensions dimensions

Figure 7: Regression-based correction pipeline

2.7.1. Regression-based correction

For both corrections, two parametric regression models were used: simple linear regression and polynomial regression. In parametric regression, the number of parameters is finite and a specific functional form is assumed in advance to describe the relationship between variables (Mahmoud, 2019).

2.7.2. Performance metrics

For each regression, the correlation coefficient is extracted. In order to assess the performance of the latter, the root mean square error (RMSE) and the mean absolute error (MAE) are calculated before and after the correction. The RMSE is defined by :

RMSE =
$$\sqrt{\frac{1}{n} \sum_{i=1}^{n} (y_i - \hat{y}_i)^2}$$
 (16)

and the MAE is calculated by:

$$MAE = \frac{1}{n} \sum_{i=1}^{n} |y_i - \hat{y}_i|$$
 (17)

3. Experimental results

3.1. t-SNE and DBSCAN results

Subsequent to the dimensional reduction of the data, the DBSCAN clustering methodology was implemented with a view to averting time leakage and overestimation of the performance model during the training of the data. The t-SNE reveals a structured organization with localized concentrations of points (Fig.8). These aggregations of points serve to emphasize images that exhibit analogous characteristics. Furthermore, within the reduced space, point aggregations are distinguished from others by the absence of apparent continuity.

Applying the DBSCAN algorithm to the dimensionally reduced data resulted in 53 distinct clusters. The DBCV (Density-Based Clustering Validation) score of 0.98 indicates highly compact and well-separated clusters. Visual inspection of clusters 33, 45, and 52 highlights tow distinct phenomena: a clear separation between upstream and downstream camera scenes, and a temporal separation of scenes from the same camera based on the presence of anthropogenic debris (Fig.8). Cluster 33 includes only upstream images, while cluster 45 and 52 contain downstream scenes, each showing different debris compositions. This suggests that images from the same scene can be found in the same data set (Fig.8) rather than several data sets; thus reducing the risk of temporal data leakage.

As previously stated, clusters were separated into three groups: train, validation, and test, with the following proportions: 80%, 10%, 10% respectively. At first, the t-SNE reveals that no cluster was separated into two different groups, which means that all images from the same cluster are actually in the same sub-dataset (Fig.8).

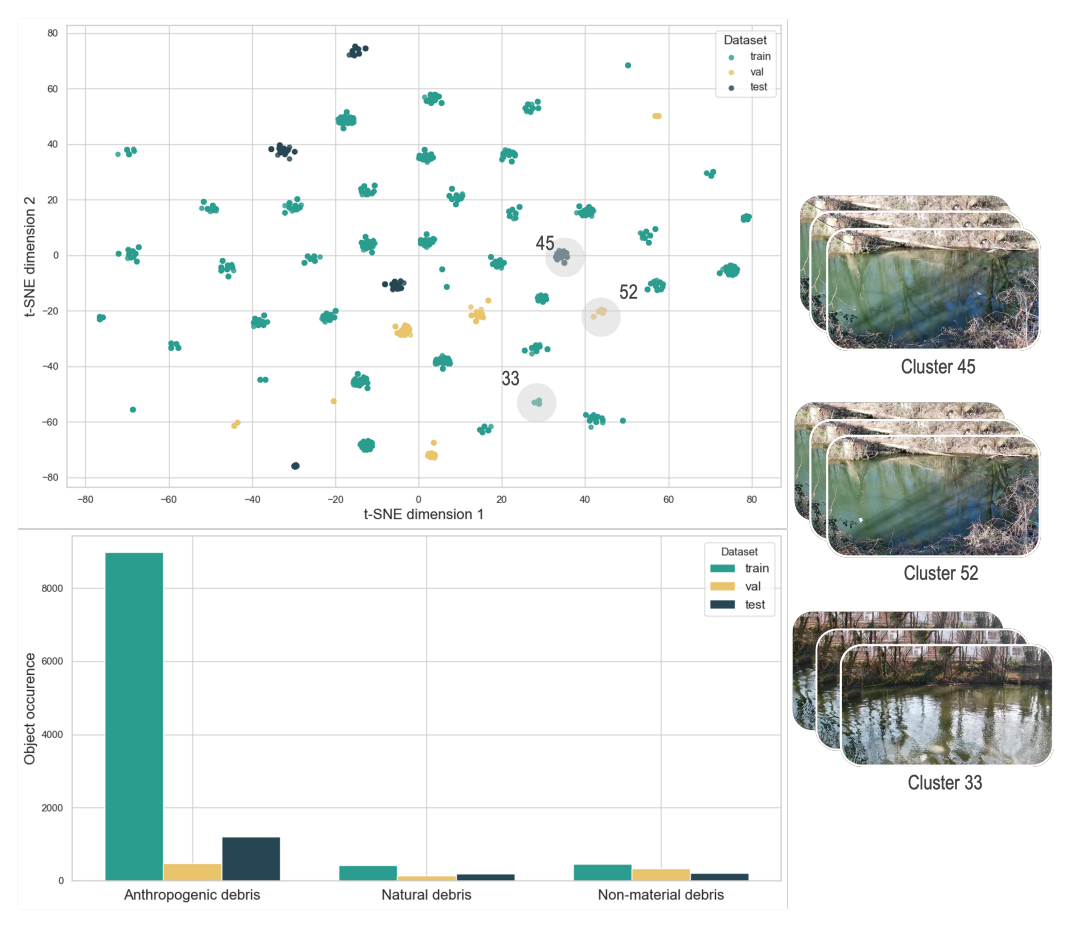


Figure 8: Clusters applied to dimensionally reduced data, occurrence of object classes in each dataset (Train, Validation, Test) and visual examples of clusters 33, 45 and 52

3.2. Object detection models benchmark

3.2.1. Training results

In this study, ten configurations were evaluated, including YOLOv5, YOLOv8, and YOLOv11 models with nano- and medium variants. In addition, for the YOLOv8-n and YOLOv11-m models, a training procedure was implemented. This involved the integration of 30% of negative images, followed by a second training run using the second dataset resulting from dimension reduction and clustering.

Among trainings 1 to 6, with an initial examination of the technical characteristics (Tab.1), Train 6 (YOLOv11-m) had the longest training time (21.508 hours for 134 epochs) while Train 1 (YOLOv5-n) was the fastest

(2.085 hours for 80 epochs). With regard to time inference performance, Train 1 was identified as the most efficient (135.27 ms for 7.39 FPS) on CPU, while Train 6 was found to be the least efficient (537.08 ms for 1.86 FPS). Concerning performance metrics (Tab.2), Train 4 (YOLOv8-m) and Train 6, have the best mAP@50 (0.965) and mAP@50-95 (0.747) respectively. In another hand, Train 1 has the lowest mAP@50 (0.933) and mAP@50-95 (0.655). This indicates that Train 4 and 6 demonstrate optimal performance in detecting and localising objects within images, whereas Train 1 exhibits the greatest difficulty. Furthermore, Train 4 and Train 3 (YOLOv8-n) have the best recall (0.942) and precision (0.97) respectively while Train 1 have the worst recall (0.885) and Train 5 (YOLOv11-m) the worst precision (0.925).

Among the six trained models, two were selected for further analysis: Train 3 and Train 6. This selection was based on a trade-off between detection performance and CPU inference time, with a view to future deployment on devices like Raspberry Pi. Train 1, despite its high inference speed (135.27 ms for 7.39 FPS), showed limited detection performance. Train 2 (YOLOv5-m) obtained good detection results, but was too slow (466.17 ms for 2.15 FPS). Train 4 achieved excellent precision (0.954) and recall (0.942), but its inference time (517.54 ms for 1.93 FPS) and the marginal gain of mAP@50 (0.965 compared with 0.962 for train 6) did not justify its selection. Train 5 offers good detection performance, but lags behind Train 6 in terms of metrics and precision (0.925) compared with Train 3 (0.970), although it is faster than Train 3 in terms of inference (137.10 ms vs. 143.12 ms).

Finally, Train 6 was selected for its strong overall metrics (Tab.2). Though slower (537.08 ms for 1.86 FPS), it is well-suited for robust, out-of-board detection. Train 3 was chosen as a balanced option for embedded applications, with good metrics (Tab.2) and efficient inference (Tab.1).

Train	Model	Epoch	Proc. time (h)	Inf. time CPU (ms)	FPS CPU
1	yolov5n	80	2.085	135.27	7.39
2	yolov5m	104	11.234	466.17	2.15
3	yolov8n	87	2.332	143.12	6.99
4	yolov8m	112	14.537	517.54	1.93
5	yolov11n	104	3.312	137.10	7.29
6	yolov11m	134	21.508	537.08	1.86
7	yolov8n-30neg	186	7.081	136.23	7.34
8	yolov11m-30neg	112	24.692	549.80	1.82
9	yolov8n-cluster	26	0.679	142.33	7.03
10	yolov11m-cluster	39	6.080	560.82	1.78

Table 1: Technical drive characteristics of models

Train	Model	mAP50	mAP50-95	Recall	Precision
1	yolov5n	0.933	0.655	0.885	0.936
2	yolov5m	0.951	0.708	0.908	0.949
3	yolov8n	0.939	0.672	0.888	0.970
4	yolov8m	0.965	0.728	0.942	0.954
5	yolov11n	0.946	0.694	0.912	0.925
6	yolov11m	0.962	0.747	0.937	0.955
7	yolov8n-30neg	0.958	0.713	0.933	0.962
8	yolov11m-30neg	0.936	0.720	0.929	0.922
9	yolov8n-cluster	0.608	0.318	0.562	0.757
10	yolov11m-cluster	0.631	0.371	0.588	0.695

Table 2: Model performance metrics

3.2.2. YOLOs trained with the negative images dataset

In this section, the training process with the YOLOv8-n and YOLOv11-m models used a dataset comprising the initial dataset and 30% of the total negative images. These trainings address the hypothesis that negative images reduce false positives in the model's detection.

The results for the YOLOv8-n model show a slight improvement in performance from Train 3 to Train 7 across all evaluation metrics (Fig.9). In the confusion matrices, class 1 (anthropogenic debris) maintains a high true positive (TP) rate, increasing marginally from 0.97 to 0.98. Class 2 (natural debris) shows a more notable gain, with TP rising from 0.82 to 0.92. Class 3 (non-debris materials) is detected perfectly in both cases (1.00). However, false positives (FP) change very little. Class 1 continues to account for the majority of FPs (increasing slightly from 0.85 to 0.86), class 2 remains steady at 0.14 and class 3 drops from 0.01 to 0. This improvement is also evident in the precision-recall (PR) curves: mAP@50 increases from 0.949 to 0.973. Class 2 shows the most significant improvement in mAP@50, rising from 0.877 to 0.940. Class 1 also shows an increase, from 0.974 to 0.983, while class 3 maintains its high level of mAP@50 at 0.995. The F1-confidence curves confirm this trend. The maximum F1-score across all classes rises from 0.93 (at a confidence threshold of 0.465) to 0.96 (at 0.436). This suggests that Train 7 provides more reliable and stable predictions.

The results for the YOLOv11-m model show no improvement in performance from Train 6 to Train 8 (Fig.10). Class 1 maintains a TP rate of 0.99 and class 3 is predicted perfectly (TP rate of 1.00), but class 2 shows a drop in TPs from 0.92 to 0.86. The number of false positives remains largely unchanged across training iterations (class 1: 0.87; class 2: 0.13 to 0.12; class 3: 0.01 to 0.00). This decline is reflected in the PR curves, with mAP@50 decreasing from 0.976 to 0.959. While class 3 retains a stable mAP@50 of

0.995, the metrics for classes 1 and 2 decline. The F1-confidence curve confirms this trend, showing that the maximum F1-score drops from 0.97 (at a threshold of 0.360) to 0.94 (at 0.481). These results suggest that incorporating negative images into YOLOv11-m training had a negative impact on its overall performance.

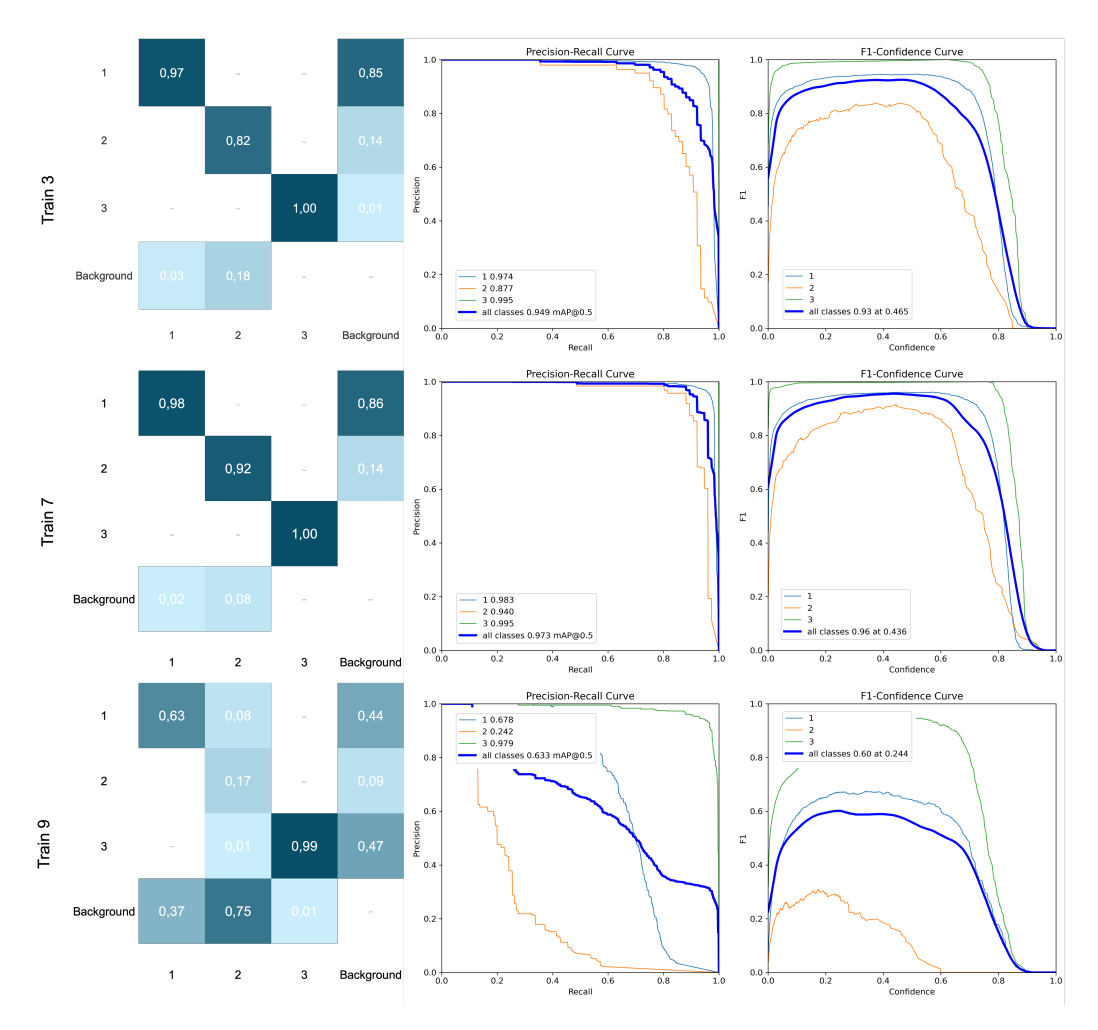


Figure 9: YOLOv8-n training results where 1= Anthropogenic Debris ; 2= Natural Debris ; 3= Non-Material Debris

3.2.3. YOLOs trained with dimensionally reduced and clustered data

Training the models with a dataset without data leakage addresses the problem of over- or under-interpretation of their performance metrics.

Training the YOLOv8-n model without data leakage (Train 9) readjusted its performance metrics (Fig.9). While the TPs for class 3 did not decrease significantly (from 1.00 to 0.99), the TPs for classes 1 and 2 decreased dramatically (from 0.97 to 0.63 and from 0.82 to 0.17, respectively). Previously (Train 3 and 7), FPs were mainly established between classes and the background. In other words, the model detected objects in the image where there were none. In Train 9, in addition to this trend, there were 0.08 FPs between anthropogenic and natural debris, and 0.01 FPs between natural debris and non-debris material. This indicates confusion between the classes themselves. This downward trend is reflected in the PR curves, where mAP@50 drops from 0.949 to 0.633. The same is true of the mAP@50 for all classes, notably the second class (dropping from 0.877 to 0.242). Overall performance is also impacted, with a decrease in the maximum F1 score from 0.93 (with a confidence threshold of 0.465) to 0.60 (with a confidence threshold of 0.244).

Training the YOLOv11-m model (Train 10) without data leakage produces identical results (Fig.10). While class 3 is unaffected, the TP rates for classes 1 and 2 decrease from 0.99 and 0.92 to 0.73 and 0.41, respectively. There is still confusion between the classes themselves and the background. As with YOLOv8-n, the PR curves (mAP@50 down from 0.976 to 0.763) and the F1-confidence curves (F1-score down from 0.97 to 0.75) illustrate this downward trend for YOLOv11-m.

However, training without data leakage has adjusted the performance metrics for YOLOv11-m less significantly than for YOLOv8-n. This can be seen in the PR curves, where mAP@50 is 0.763 for YOLOv11-m (Fig.10) and 0.633 for YOLOv8-n (Fig.9). The same is true of the F1 score: 0.60 with a confidence threshold of 0.244 for YOLOv8-n (Fig.9), and 0.75 with a confidence threshold of 0.249 for YOLOv11-m (Fig.10). Thus, training without data leakage has enabled the metrics to be adjusted to reflect the actual performance of the models. Nevertheless, YOLOv11-m appears to perform better than YOLOv8-n.

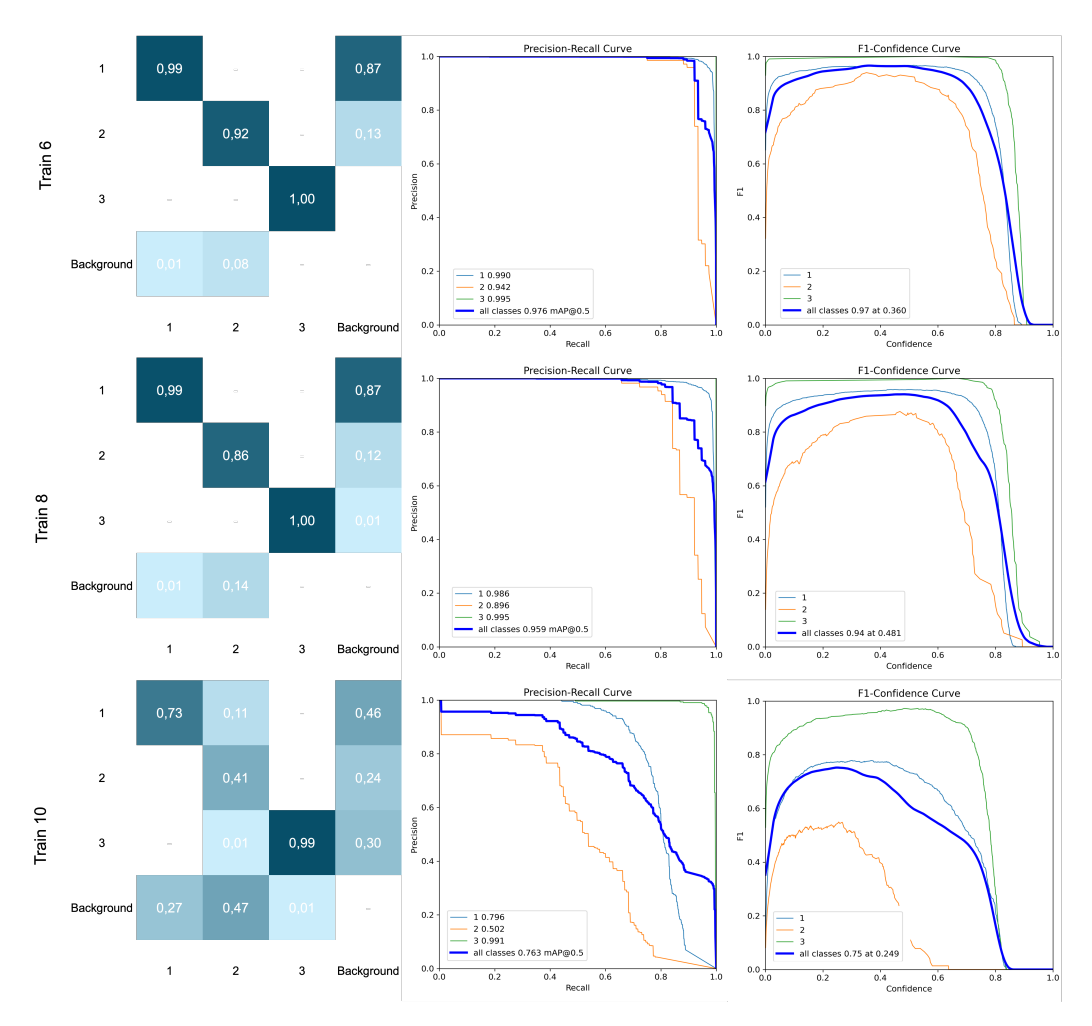
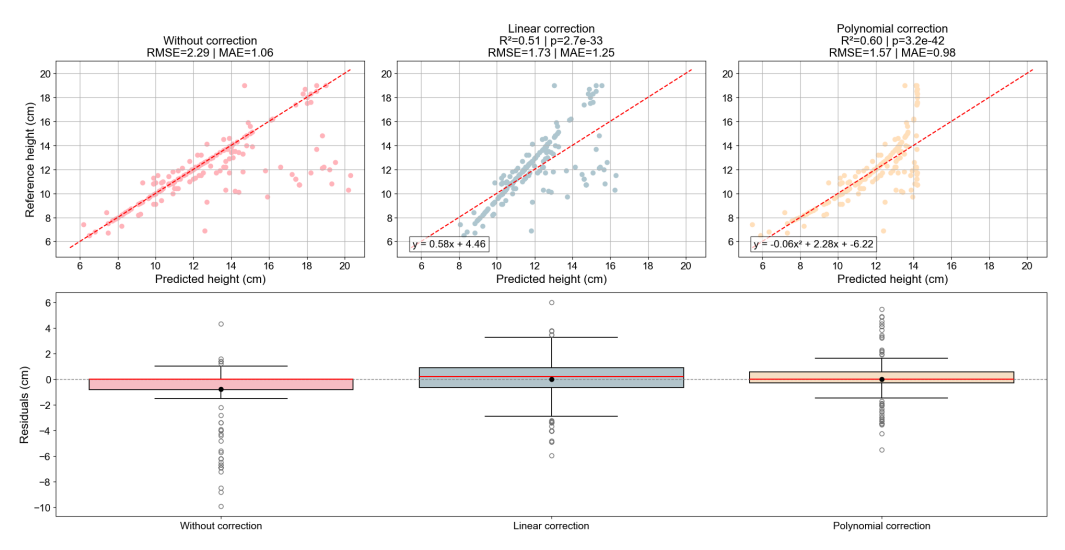


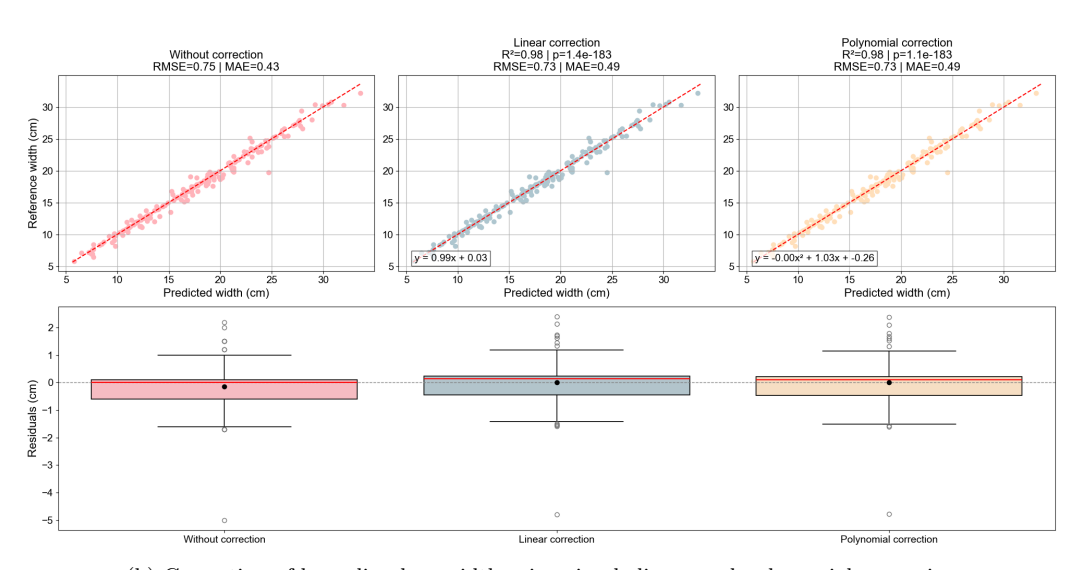
Figure 10: YOLOv11-m training result where 1= Anthropogenic Debris ; 2= Natural Debris ; 3= Non-Material Debris

3.3. Regression-based correction

3.3.1. Predicted bounding box shape correction



(a) Correction of bounding box height using simple linear and polynomial regression



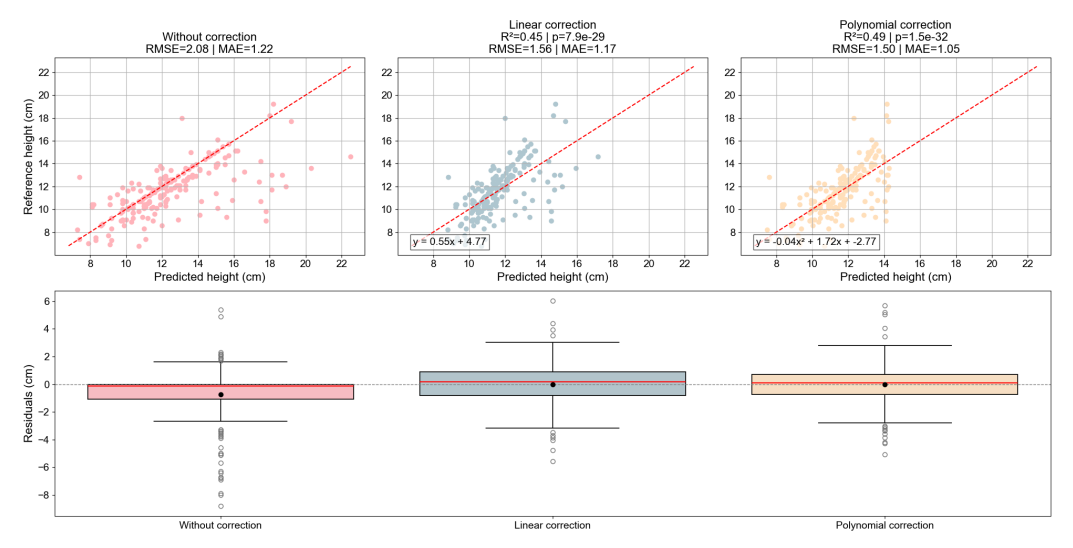
(b) Correction of bounding box width using simple linear and polynomial regression

Figure 11: YOLOv11-m (Train 6) bounding box shape correction

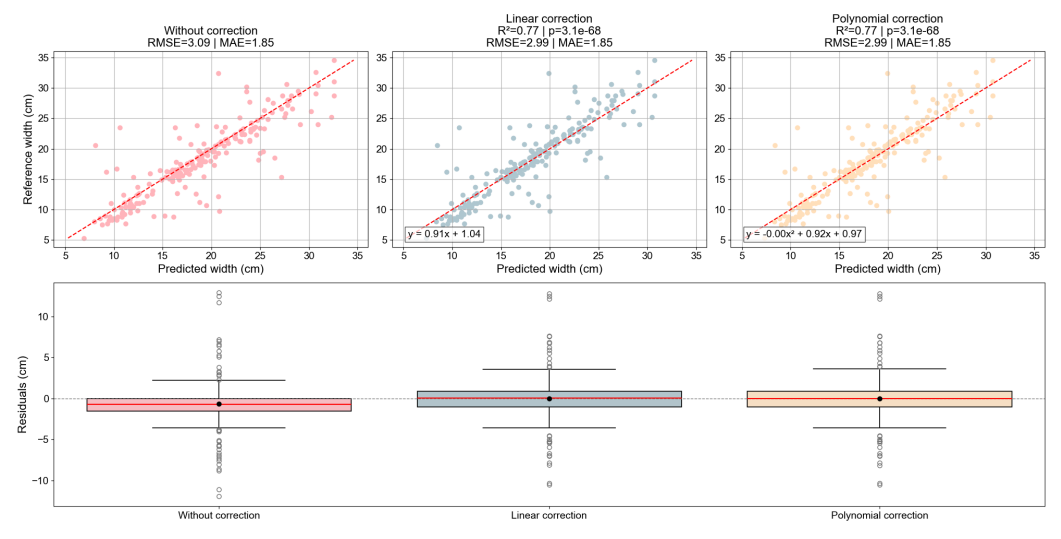
The application of a correction to the YOLOv11-m model (Train 6) has been demonstrated to enhance the accuracy of the predicted bounding box

heights (Fig.11a). In the absence of correction, predictions are found to be biased, as evidenced by the RMSE measuring at 2.29 cm and the MAE at 1.06 cm. This bias is characterised by a propensity to overestimate, as demonstrated by the residuals exhibiting a skewness towards negative values, with a median of 0 cm and a mean of -0.78 cm. Linear regression reduces errors (RMSE = 1.73 cm; MAE = 1.25 cm), but polynomial regression performs better, lowering RMSE to 1.57 cm and MAE to 0.98 cm. The residuals become more centred and symmetrical (median = -0.02 cm; mean = 0 cm), with reduced and balanced extremes (-4 cm to 5 cm). In a similar manner, polynomial regression enhances predictions for the YOLOv11-m (Train 10 without data leakage) (Fig.12a), leading to a reduction in RMSE from 2.08 cm to 1.50 cm and MAE from 1.22 cm to 1.05 cm. In comparison, the gains yielded by linear regression are more limited (RMSE = 1.56 cm; MAE = 1.17 cm). As was the case with Train 6, initial predictions demonstrate a propensity to overestimate heights (median = -0.15 cm; mean = -0.75 cm). However, this tendency is rectified by the polynomial fit, which centres the residuals (median = 0.08 cm; mean = 0 cm).

For the YOLOv11-m model (Train 6), the correction results for width predictions are contrasted (Fig.11b). Prior to the implementation of the correction, the errors were already minimal (RMSE = 0.75 cm; MAE = 0.43 cm). The results reveal that neither linear nor polynomial regression significantly improves performance, with both methods reducing RMSE to 0.73 cm, but increasing MAE to 0.49 cm. This suggests that there is no clear benefit from the implementation of either regression method. In a similar manner, for Train 10 (Fig.12b), both regression types reduced the RMSE from 3.09 cm to 2.99 cm, while the MAE remained stable at 1.85 cm. Despite the average error remaining relatively constant, the decline in RMSE indicates a reduction in outliers. This finding is corroborated by the residual extremes, which shift from -12 cm / +13 cm prior to correction to -10 cm / +12 cm following the implementation of either regression, thereby indicating a marginal reduction in the most extreme prediction errors.



(a) Correction of bounding box height using simple linear and polynomial regression



(b) Correction of bounding box width using simple linear and polynomial regression

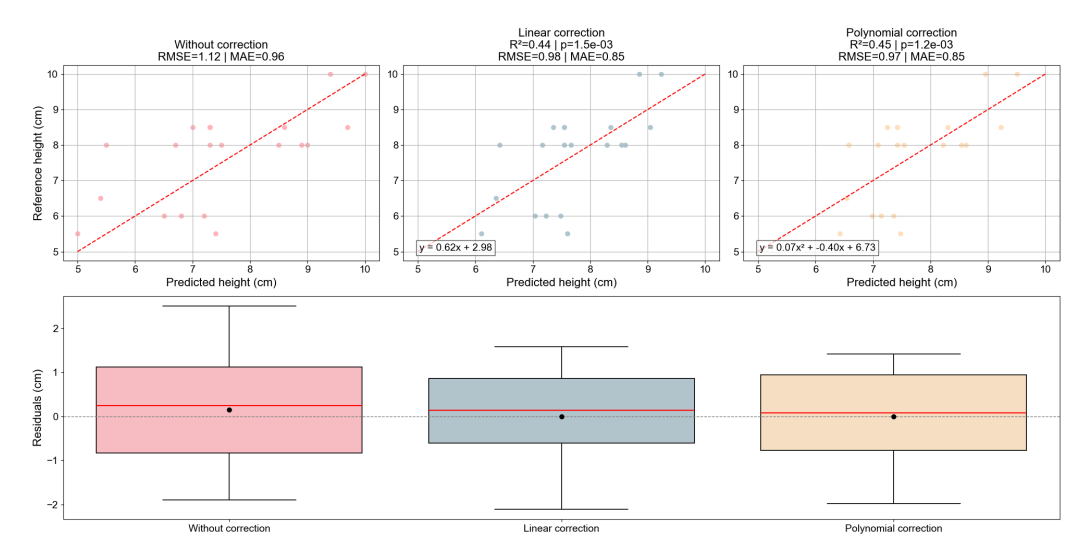
Figure 12: Data leak-free YOLOv11-m (Train 10) bounding box shape correction

3.3.2. Bounding box dimensions correction

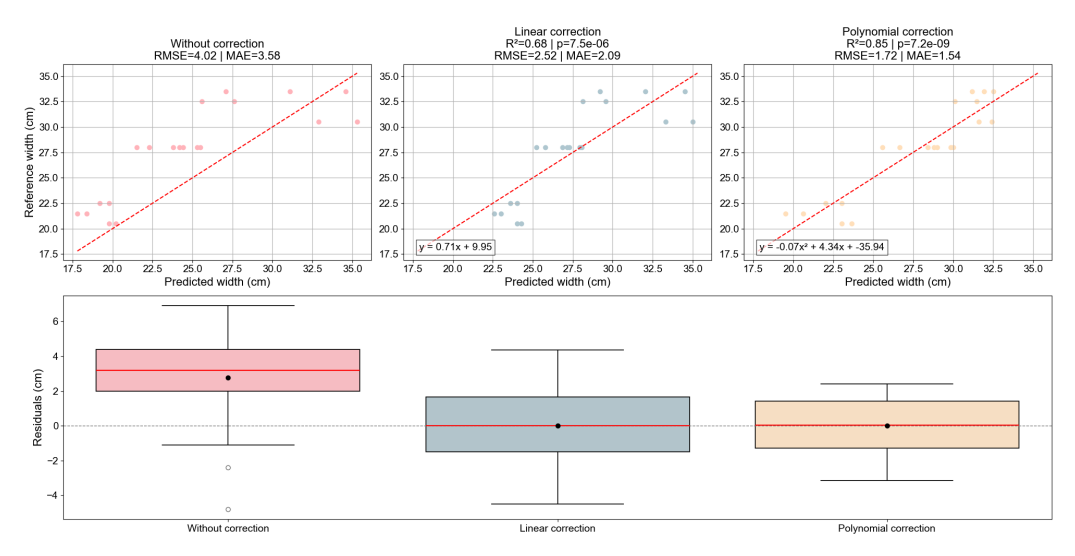
Without correction, height predictions demonstrate moderate errors (RMSE = 1.12 cm; MAE = 0.96 cm) and fairly dispersed residuals (Q1 = -0.82 cm; Q3 = 1.12 cm) (Fig. 13a). The efficacy of both correction methods is comparable, with linear regression reducing the root mean square error (RMSE) to

0.98 cm and polynomial regression to 0.97 cm. In both cases, the mean absolute error (MAE) remains consistent at 0.85 cm. The residuals were found to be marginally more centred, and the linear regression model achieved the optimal reduction in the interquartile range (Q1 = -0.61 cm; Q3 = 0.86 cm). The results indicate that both corrections offer only marginal enhancements in terms of prediction accuracy.

In contrast, width predictions benefit more substantially from correction (Fig. 13b). Simple linear regression achieves an RMSE of 2.52 cm and a MAE of 2.09 cm. However, polynomial regression yielded optimal results, reducing the RMSE from 4.02 cm to 1.72 cm and the MAE from 3.58 cm to 1.54 cm. Prior to the implementation of the correction, the residuals exhibited a marked skewness towards positive values (median = 3.2 cm; mean = 2.76 cm), thereby indicating a systematic underestimation of the actual widths. It is evident that polynomial regression effectively recenters these residuals (median = 0.03 cm; mean = 0 cm), thereby significantly improving prediction accuracy.



(a) Bounding box height dimension correction by simple linear and polynomial regression



(b) Bounding box width dimension correction by simple linear and polynomial regression

Figure 13: Bounding box dimensions correction

3.3.3. Object size prediction with corrections applied

For this final experiment, we adopt an end-to-end evaluation of the complete pipeline. The YOLOv11-m (Train 6 and 10) models, identify bounding boxes on which a shape correction is applied (Section 3.3.1). Subsequently, the geometric model estimates the corresponding object sizes, which are

further refined using the method described in Section 3.3.2. These results demonstrate how the combined corrections influence the overall estimation in a realistic setting. Table 3 and 4 summarizes the mean absolute error (MAE) and root mean square error (RMSE) obtained for each correction strategy. This provides a quantitative comparison of their respective impacts on estimation accuracy.

The YOLOv11-m model trained with data leakage (Train 6; Tab.3) outperforms the leakage-free version (Train 10; Tab.4) in terms of raw and corrected error metrics. For width predictions, Train 6 achieves RMSEs of 1.81 cm (individual correction) and 1.77 cm (pipeline correction) (Tab.3a), compared to 2.23 cm and 2.14 cm, respectively, for Train 10 (Tab.4a). For height predictions, Train 6 achieves RMSEs of 1.83 cm (individual) and 1.86 cm (pipeline) (Tab.3b), whereas Train 10 achieves 2.18 cm (individual) and 1.68 cm (pipeline) (Tab.4b). Overall, corrections appear to be more effective on Train 6. However, this is to be expected: the presence of data leakage inflates performance metrics, creating a false impression of generalisation ability. Therefore, the metrics from Train 6 are biased, whereas those from Train 10 more accurately reflect the model's true performance.

Analyzing YOLOv11-m without data leakage allows us to see how effective each box shape and box dimension correction is and how double correction strategies reduce error. The best width (Tab.4a) and height (Tab.4b) predictions are achieved with linear regression applied to the dimension itself (Width: RMSE = 2.23 cm; MAE = 1.71 cm / Height: RMSE = 2.18 cm; MAE = 1.62 cm). For combined corrections, the most effective pipeline for width prediction uses polynomial regression for box shape and dimension corrections, yielding an RMSE of 2.14 cm. The best MAE (1.65 cm) is obtained using a pipeline that combines simple linear regression for box shape correction and polynomial regression for dimension correction. For height prediction, the optimal pipeline applies polynomial regression to box shape correction, followed by linear regression to correct the dimensions, achieving the best RMSE (1.68 cm) and MAE (1.48 cm).

Overall, geometric-level correction on its one is more efficient of box-level correction only. However, double level correction reaches better RMSE and MAE than one level correction. For width prediction, the best combination appears to be the correction pipeline with polynomial box shape-level and polynomial box dimension-level. For height predictions, however, the more efficient pipeline is the combination of polynomial box shape-level and simple linear box dimension-level correction.

(a) Width (cm)

	No Dim Corr		Dim Corr (Lin)		Dim Corr (Poly)	
	RMSE	MAE	RMSE	MAE	RMSE	MAE
No Box Shape Corr	2.83	2.38	1.86	1.27	1.81	1.53
Box Shape Corr (Lin)	3.02	2.60	1.84	1.30	1.77	1.49
Box Shape Corr (Poly)	2.47	1.98	1.97	1.34	1.99	1.78

(b) Height (cm)

· · · · · · · · · · · · · · · · · · ·							
	No Dim Corr		Dim Corr (Lin)		Dim Corr (Poly)		
	RMSE	MAE	RMSE	MAE	RMSE	MAE	
No Box Shape Corr	2.59	1.68	1.83	1.35	2.84	1.78	
Box Shape Corr (Lin)	2.56	2.06	1.89	1.52	2.50	1.92	
Box Shape Corr (Poly)	2.70	1.85	1.86	1.34	2.87	1.93	

Table 3: RMSE and MAE (in cm) under different correction strategies separately for width and height predictions for YOLOv11-m (Train 6). Blue metrics are the lowest RMSE and MAE for individual corrections and red metrics are the lowest RMSE and MAE for pipeline corrections.

(a) Width (cm)

	No Dim Corr		Dim Corr (Lin)		Dim Corr (Poly)	
	RMSE	MAE	RMSE	MAE	RMSE	MAE
No Box Shape Corr	3.16	2.65	2.23	1.71	2.36	2.02
Box Shape Corr (Lin)	3.95	3.57	2.23	1.90	2.16	1.65
Box Shape Corr (Poly)	3.91	3.52	2.23	1.89	2.14	1.66

(b) Height (cm)

	No Dim Corr		Dim Corr (Lin)		Dim Corr (Poly)	
	RMSE	MAE	RMSE	MAE	RMSE	MAE
No Box Shape Corr	3.57	2.27	2.18	1.62	5.80	2.84
Box Shape Corr (Lin)	2.86	2.38	1.91	1.64	3.26	2.38
Box Shape Corr (Poly)	2.55	2.17	1.68	1.48	2.83	2.17

Table 4: RMSE and MAE (in cm) under different correction strategies separately for width and height predictions for YOLOv11-m (Train 10). Blue metrics are the lowest RMSE and MAE for individual corrections and red metrics are the lowest RMSE and MAE for pipeline corrections.

To contextualize these results, we introduce the *per-pixel sensitivity* metric, which quantifies the effect of a one-pixel shift in the bounding box on the estimated object size.

$$S_{\text{pixel}}^{(d)} = \frac{1}{N} \sum_{i=1}^{N} \left| \hat{s}_i - \hat{s}_i^{(d)} \right|$$
 (18)

Here, \hat{s}_i is the estimated size (width or height) of the *i*-th object using the original bounding box, and $\hat{s}_i^{(d)}$ is the estimated size when the bounding box is shifted by one pixel in direction d, where $d \in \{\text{left}, \text{right}, \text{top}, \text{bottom}\}$. The metric $S_{\text{pixel}}^{(d)}$ represents the average absolute change in predicted size over all N samples due to this one-pixel perturbation.

This provides a resolution-based lower bound on the estimation error: achieving a lower error than $S_{\text{pixel}}^{(d)}$ would imply subpixel precision, which is beyond what is expected from a typical image processing algorithm.

beyond what is expected from a typical image processing algorithm. By computing $S_{\text{pixel}}^{(d)}$ for the camera's horizontal and vertical axes on the same dataset, we obtain an average per-pixel sensitivity of **1.34** cm for the

object width and 1.36 cm for the object height.

These values serve as a natural benchmark to interpret the observed RMSE and MAE. Since the reported errors are not substantially greater than these sensitivity thresholds, it indicates that the proposed method leverages nearly all the spatial information available in the input. In practice, this means that the estimated object sizes are nearly as precise as what is physically achievable given the image resolution, leaving little room for further improvement without higher-resolution input data.

4. Discussion

4.1. Influence of dataset bias, integrity, and composition on deep learning models

4.1.1. Unbalanced dataset

A common issue in CNN training is class imbalance, which occurs when one class dominates the dataset while the others are significantly underrepresented (Ghosh et al., 2024). This imbalance causes the model to prioritise the detection of the dominant class during training (Pulgar et al., 2017), ultimately leading to a decline in overall performance (Masko and Hensman, 2015). Despite containing 6,013 images, our dataset is highly imbalanced, with 10,873 instances of anthropogenic debris compared to just 755 instances of natural debris and 1,010 instances of non-debris materials. This imbalance, combined with limitations in data quality and setup, reduces the model's reliability (Gong et al., 2023). It also severely affects the model's ability to generalise, particularly with regard to underrepresented classes (Johnson and Khoshgoftaar, 2019). This highlights the need for larger, more balanced and diverse datasets in order to develop robust and reliable detection models (Munappy et al., 2022).

In this study, this shortcoming is due in particular to in situ data acquisition slowed down by time-consuming manual annotation work (on LabelImg). A number of approaches can overcome this problem. Self-supervised models (SSL) are increasingly used to build large datasets (Jaiswal et al., 2020). Since it does not require annotated data, the SSL model can learn the major characteristics of the input data. Once the model is pre-trained, it can be reused in a downstream task - such as classification or detection - via a fine-tuning process on a smaller annotated dataset (Gui et al., 2024). Recently, the use of embeddings from giga-models has emerged as a major breakthrough in deep learning, as it allows models to converge both faster

and more effectively. Over the past few months, several notable developments have been introduced, such as AlphaEarth (Brown et al., 2025) for remote sensing data and DINOv3 (Siméoni et al., 2025) for photographs, which can enhance performance and reduce false positives for our task.

4.1.2. Contribution of negative images and effect on the number of false positives

Object detection in river environments is particularly challenging due to the complexity of captured scenes. Images taken from fixed cameras on riverbanks, onboard USVs (unmanned surface vehicles; (Bovcon et al., 2021)) or boats (Armitage et al., 2022) are often affected by water reflectivity, producing glare or mirror-like effects depending on lighting (Yalçın and Ekenel, 2024). These biases frequently result in false positives, as shown in confusion matrices (Fig.9 and 10). To mitigate this issue, we hypothesised that including negative images (background only) could reduce false positive rates. Negative samples were selected under varied environmental conditions: one cloudy day and one bright, clear-sky day at different times of day. Considering the complex variations that are established in the filmed environment then enables the model to extract more varied background features to account for changing background conditions (Gao et al., 2019).

To reduce false positive rates due to confusion between anthropogenic debris and the river environment, studies are exploring architectural modifications to the models (Chang et al., 2024; Tao et al., 2024; Wang and Zhao, 2024) while our work focuses on improving the datasets. The performance of our YOLOv8-n (Train 7) and YOLOv11-m (Train 8) models falls within the range reported in the literature for similar tasks. Compared to YOLOv8-MSS (Wang and Zhao, 2024), a model optimised for small object detection through additional dedicated heads (mAP@50 = 87.9%; mAP@50-95 = 47.6%), Train 7 (mAP@50 = 95.8%; mAP@50-95 = 71.3%) and Train 8 (mAP@50 = 93.6%; mAP@50-95 = 72%) achieve superior results. Other models, such as DSFLDNet, for Dense Small Floating Litter Detection Network, (mAP@50 = 97.3%; recall = 93.9%), which is based on a multidimensional attention mechanism that combines the spatial and frequency domains of the image (Ye et al., 2025), show a similar level of performance to that of Train 7 (recall = 93.3%) and Train 8 (recall = 92.9%).

The models trained with negative images show similar performance trends to those reported in the literature, but the outcome of adding negative images is mixed. In the case of YOLOv8-n, their inclusion led to a slight improvement in performance (Tab.1 - Train 3 vs. Train 7). However, this trend was not observed for YOLOv11-m (Tab.1 - Train 6 vs. Train 8). Additionally, incorporating negative images significantly increased processing time, from 2.332 hours to 7.081 hours for YOLOv8-n and from 21.508 hours to 24.692 hours for YOLOv11-m. Moreover, the expected reduction in false positives is restricted to YOLOv8-n and is not observed for YOLOv11-m (Fig.9 and 10).

The differential impact of adding negative images between YOLOv8-n and YOLOv11-m training may stem from the difference between the two architectures. The YOLOv8-n model, being a simpler model (72 layers and 3,006,233 parameters in this study), is more sensitive to background noise and can better benefit from the negative images in the dataset to better distinguish objects from the image background. In contrast, the YOLOv11-m model has a more complex architecture (123 layers and 20,032,345 parameters in this study) and incorporates modules to improve its ability to target regions of interest in the image and therefore place less emphasis on the background (Alif and Hussain, 2024; Khanam and Hussain, 2024). As a result, negative data can introduce redundancy or even noise into the training of this model, which can then reduce its detection performance.

4.1.3. Effect of training on the leak-free dataset

In machine learning (ML), data leakage occurs when some of the data in the training set also appears in the validation or test sets (Tampu et al., 2022; John et al., 2025). While this does not directly affect the internal learning process of the model, it artificially inflates performance metrics, providing an inaccurate impression of the model's effectiveness in real-world scenarios (Apicella et al., 2024). Leakage can arise from pre-processing steps or from the inherent structure of the data itself (Seide et al., 2011). In the present study, image data are extracted from continuous video footage capturing the periodic occurrence of anthropogenic and natural debris as well as non-debris material. Similar images from the same temporal scene can be found in both training and test sets when the dataset is split into three parts (training, validation and test; (Bouke and Abdullah, 2023)), as was the case from Train 1 to 8.

As the data is acquired in the form of video time series, the objective of distinguishing images from different recording scenes implies their transformation into embedded vectors. These vectors combine visual features extracted using a YOLOv8-n encoder, bounding box information and the

corresponding timestamps. This representation reduces the dimensionality of the data while retaining its semantic richness (Figueiredo and Mendes, 2024). A t-SNE is generated from the embedded vector (used to reduce the data's dimensionality) in order to facilitate visualisation and apply DB-SCAN clustering (Fig.8). While t-SNE is particularly well suited to data with a temporal component, other methods, such as principal component analysis (PCA), can be used for preprocessing large datasets acquired under varying conditions (i.e. scenes, objects and sensors (Sasse et al., 2025)). This method eliminates the need for additional information such as timestamps. Clustering methods can be applied to the PCA results to identify relevant groupings once the data has been projected into a reduced-dimensional space. These groupings can then be used to create separate data sets (i.e. training, validation, testing) and avoid time leaks or interset redundancies. This type of strategy is particularly useful in cases of heterogeneous acquisition (different sensors, lighting conditions, camera angles), in preparation for cross-validation procedures or successive implementations (Aarnink et al., 2025).

The CNNs that were trained using the dataset without any data leakage, namely YOLOv8-n (Training Set 9: precision = 75.7%; mAP@50 = 60.8%) and YOLOv11-m (Training Set 10: precision = 69.5%; mAP@50 = 63.1%), demonstrate lower detection performance than some of the models that have been reported in the literature. For instance, YOLOv5 models designed specifically for wood detection in rivers achieve much higher precision (99.5%; (Donal et al., 2023)). Similarly, YOLOv5 models designed for detecting anthropogenic debris report mAP@50 scores of 88% (Nunkhaw and Miyamoto, 2024) and an precision of 86% (Luo et al., 2022). However, while the models developed in this study may underperform in comparison, their metrics are more realistic as they are not inflated by data leakage. In contrast, models from the literature may produce overestimated results due to random dataset splits that do not account for spatial or temporal continuity, leading to similar images appearing in both the training and test sets. Furthermore, the robustness and generalisability of detection models depend on data acquisition conditions, such as environmental variability and sensor placement. This further supports the need for cautious interpretation of high performance metrics when data leakage risks are not explicitly addressed.

This approach is a replicable methodology for reducing data leakage when working with time-series data. In the context of a restricted dataset with little variation in recording conditions, complementary information such as bounding boxes and timestamps is necessary. For these data, we recommend using an embedded vector followed by t-SNE to differentiate between scenes and divide them into groups, creating several datasets. In case of larger and more heterogeneous datasets, it is preferable to apply PCA followed by a clustering method based solely on the visual characteristics of the images to minimise the presence of similar images in different datasets.

4.1.4. Dataset integrity and overfitting effects

A comparative analysis with a version of YOLOv11-m trained with temporal data leakage reveals the risks associated with overfitting. Although the leaked model yields lower raw error metrics (Tab.3), this performance reflects overfitting to specific objects seen during training (Babu et al., 2024). In contrast, the leak-free model generalises better to unseen data.

Crucially, our geometric and statistical correction pipeline remains stable across both detector versions, indicating robustness to upstream detection bias. The correction models do not amplify overfitting artifacts, and instead re-center predictions around realistic values. This underlines the importance of rigorous dataset partitioning and further supports the use of the cleaner and more generalizable model.

4.2. Object size prediction

In our study area, the absence of man-made structures (such as bridges) justifies the installation of cameras on the riverbank. This installation leads to geometric deformation (perspective) due to the camera's inclined position, which is not the case when a camera is fixed to a bridge (providing a vertical view; (Van Lieshout et al., 2020)). To correctly estimate the dimensions of debris, it is necessary to correct geometric distortion, thereby limiting errors in predicted heights and widths.

The proposed pipeline achieves a high level of precision in estimating real-world object dimensions, despite numerous sources of visual and geometric uncertainty in outdoor river imagery. Through the combination of a physics-based geometric correction and a statistical calibration step, the method consistently yields dimension estimates that are sufficiently accurate for downstream applications such as plastic mass estimation. This section discusses the model's robustness, underpinning assumptions, inherent and practical limitations, and perspectives for future work.

4.2.1. Geometric model and approximation assumptions

The model uses camera parameters (i.e. installation height, tilt angle, and focal length) to project bounding box coordinates from image space to physical coordinates. Without requiring any assumption on object orientation or planarity, the model achieves accurate results, especially after applying a second-degree, regression-based correction (Tab.4). For instance, width RMSE improves from 3.16 cm (uncorrected) to 2.14 cm after geometric and polynomial correction (Tab.4a), while height estimates are refined to within 1.68 cm (Tab.4b).

The model includes certain approximations that rely on simplifying geometric assumptions, which, while not strictly exact, are operationally effective. First, it assumes the object center lies along the ray passing through the center pixel of the bounding box. This assumption provides a stable basis for geometric projection in practice, even if it is not theoretically justified. Second, the object size is estimated by summing two ray-plane intersections (top/bottom and left/right). While these are only approximately valid, they yield accurate results due to the near-parallel nature of rays in the camera configuration employed.

It is worth noting that the computed *height* corresponds to the projection of the object along the camera's vertical viewing axis, not a strict vertical measurement in world coordinates. In most cases, the distinction is negligible, particularly for compact floating debris, but the difference may become relevant for extended or tilted objects (i.e. elongated wooden logs). Nevertheless, our empirical corrections compensate for such biases within the current application scope.

4.2.2. Limitations of bounding box representation and prospects for rotationaware detection

The present pipeline operates with axis-aligned bounding boxes, which introduces a practical limitation when estimating the dimensions of rotated objects (Fig.14). A tilted object enclosed in an axis-aligned bounding box results in a distorted representation: the box tends to underestimate the object's major dimension and overestimate its minor one, effectively squaring the projection. However, this is a constraint of the detector representation rather than the geometric model itself. The projection algorithm is capable of handling rotated boxes and would presumably produce correct dimension estimations given accurate angular information.



Figure 14: Example of parallel (left) and inclined (right) bottle

Recent object detectors support rotated bounding boxes (e.g., YOLOv11-OBB; (Ultralytics, 2024)), and future integration of such models is expected to entirely mitigate this limitation. Accordingly, object rotation should not be considered as a fundamental barrier but rather as a temporary constraint inherent to the current detection model. Our evaluation has therefore focused on objects oriented either horizontally or vertically to avoid bias from this artifact.

4.2.3. Error analysis and proximity to resolution limits

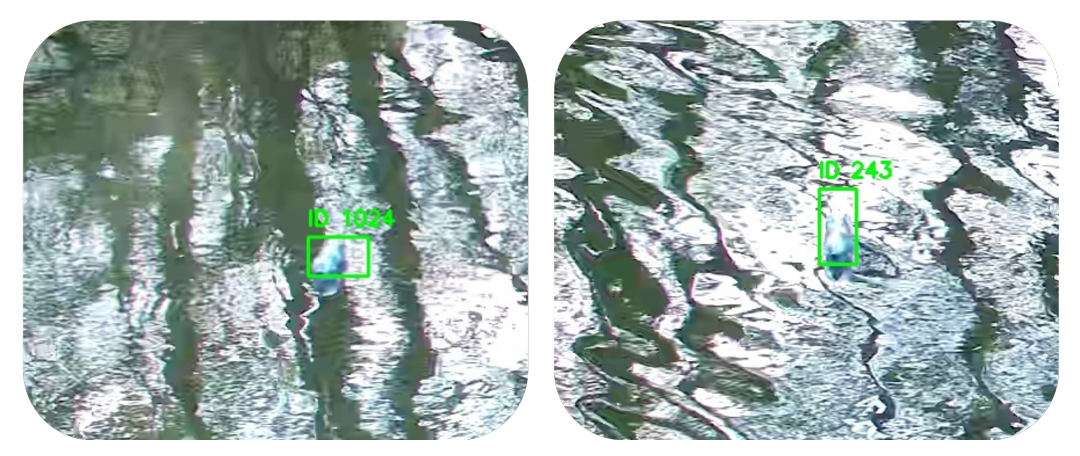
Following correction, the residual estimation errors approach the sensitivity threshold dictated by the image resolution and scene geometry. We define a per-pixel sensitivity metric—roughly 1.3 cm for both width and height under our conditions—as a lower bound on attainable precision. The final RMSEs of 2.14 cm (width) and 1.68 cm (height) for the leak-free model approach this limit, indicating that the method extracts nearly all the geometric information available from the image.

This suggests that further accuracy improvements would likely require higher-resolution sensors, more precise calibration, or alternative imaging modalities. Given that our objective is to provide a lightweight and fielddeployable system, the current error range is both satisfactory and nearoptimal in the given constraints.

4.2.4. Environmental artifacts: reflections and occlusions

Natural environments introduce unavoidable artifacts, including watersurface reflections and occlusions. Debris reflections on water surface (Yalçın and Ekenel, 2024) often extend the vertical footprint of the object in the image, leading to overestimated height predictions. Occlusions may result in truncated boxes, contributing to underestimation (Fig.15 b).

These phenomena particularly affect the Y-axis of bounding boxes and can explain some systematic biases in height estimation. While our corrections alleviate these issues to some extent, they cannot fully remove the underlying visual ambiguity. Additional methods such as temporal filtering or reflection-aware postprocessing could further improve accuracy in these scenarios.



(a) Light reflection on the surface of the water



(b) Bottles reflected on the water

Figure 15: Examples of mirror effect of water

4.2.5. Morphological asymmetries and object orientation

Shape-induced asymmetries presumably contribute to residual width estimation error. For instance, rotating a horizontally placed bottle by 180° can yield a different bounding box due to the tapering near the cap. This asymmetry, combined with axis-aligned detection, introduces a measurable variation in estimated size. Future detectors that support instance-level segmentation or rotated bounding boxes may help reduce this variability.

4.3. First spatial inference testing works of YOLOv11-m to detect plastic debris on the Bruche river

In order to broaden the findings and the scope of this study, the YOLOv11-m model (Train 10) was inferred on images obtained from the Bruche River.

The Bruche is an 80-kilometre-long Rhine sub-tributary that originates in the Vosges Mountains, and subsequently drains the Upper Rhine Graben (Jautzy et al., 2020).

A 3-megapixel pan-tilt-zoom (PTZ) camera was installed on the DREAL (Direction Régionale de l'Environnement, de l'Aménagement et du Logement) Holtzheim hydrometric station on the left bank of the river (Fig.16). A qualitative analysis of YOLOv11-m's performance on these images highlights the model's ability to detect anthropogenic debris and non-debris materials under various recording conditions. These spatial inference results are encouraging as the model was originally trained on a different river (the Steingiessen).

As previously discussed (Section 4.1.1), increasing both the volume and diversity of training data enhances detection performance. The deployment of supplementary cameras appears to be a pertinent strategy for the acquisition of such enriched datasets.

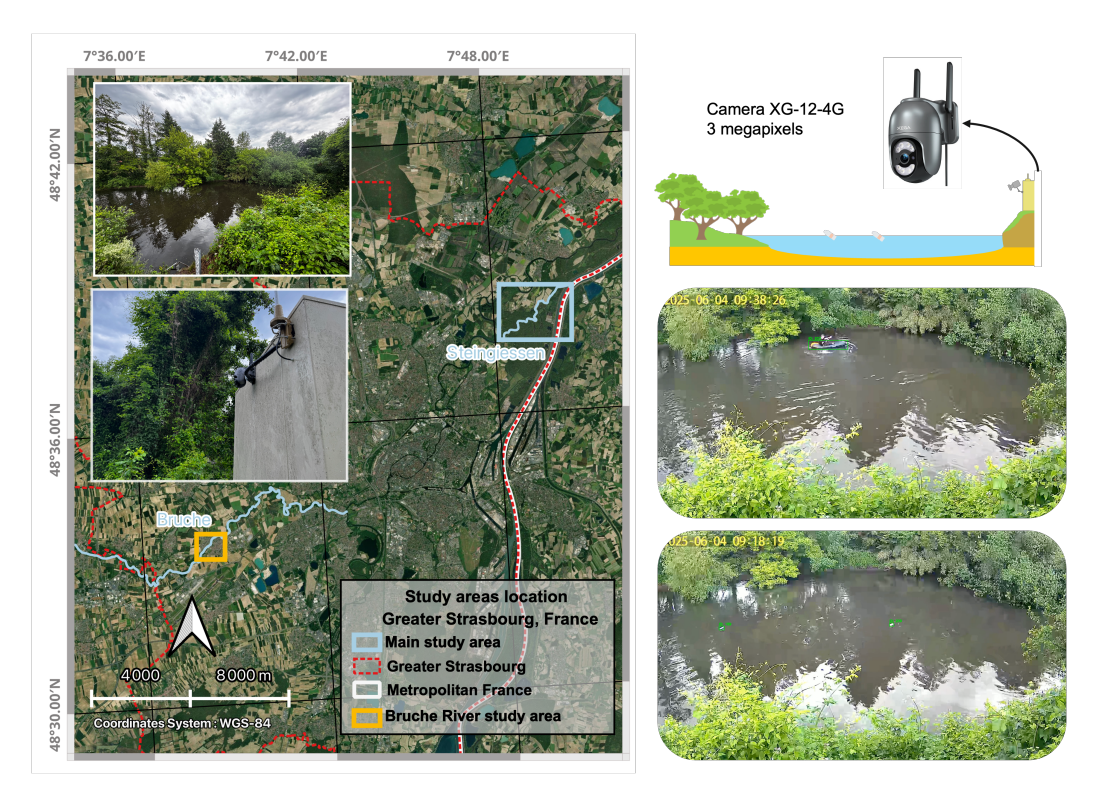


Figure 16: Spatial inference of YOLOv11-m (Train 10) model on Bruche River (South-West Greater Strasbourg)

4.4. Contribution to the Overarching Research Goal

4.4.1. Models for detecting anthropogenic debris in rivers

The benchmark method used to test different object detection models highlights two convolutional neural networks: YOLOv8-n and YOLOv11-m. The method used represents a first approach to detect floating anthropogenic debris in rivers.

The compared analysis of two models with contrasting degree of complexity in terms of architecture is a first step towards operational issues. Future studies should foster the creation of models embedded in cameras to create a tool that can be deployed at the catchment scale to quantify the global phenomenon of plastic pollution.

4.4.2. A tool for estimating the dimensions of objects detected by a monocular camera

The proposed method demonstrates that reliable, centimeter-level object dimension estimation is feasible with a monocular bank-mounted camera, provided that the imaging parameters are known and a suitable geometric model is applied. The performance is close to the theoretical limits set by image resolution and projection geometry.

By explicitly modeling perspective, correcting for biases, and acknowledging practical limitations, the pipeline offers an interpretable and effective tool to monitor riverine debris. It constitutes a robust foundation upon which future refinements—such as orientation-aware detection, reflection filtering, or mass estimation models—can be built.

4.4.3. From size to mass estimation: assumptions and limitations

While the current pipeline estimates object dimensions only, the broader goal is to infer plastic mass or volume. The implicit assumption is that object size correlates with plastic content, particularly for bottles. This is a reasonable first approximation; however, it may not hold for atypical objects or classification errors. For example, a kayak misclassified as a large plastic item could substantially bias aggregate mass estimates.

In future work, size-based consistency checks will be incorporated to reject implausible combinations of classification and dimension. More refined estimations would also benefit from integrating material recognition or object-type-specific volume models.

5. Conclusion

This study proposes an innovative and reproducible approach for monitoring anthropogenic floating waste in river, combining deep learning detection and geometric modelling. The deployment of in situ cameras on riverbanks enables the system to acquire images in a complex natural and urban environment on a continuous basis. The integration of negative data, the consideration of data leakage biases, and the rigour of the annotation and dataset creation protocol have optimised the robustness of the results. The methodological framework offers a promising tool for the long-term monitoring of plastic pollution in urban and natural river environments. Furthermore, it facilitates the integration of automated, low-cost monitoring systems. These systems can be adapted on a large scale.

A comparative evaluation of several variants of YOLO models identified two convolutional neural networks that are particularly well suited to the river context: YOLOv8-n and YOLOv11-m. Despite the presence of variable recording conditions, these models demonstrated effective performance in object detection. A detailed performance analysis, particularly using datasets free of temporal leakage, highlights the importance of a rigorous protocol in the construction of training datasets. The incorporation of negative images enhanced the accuracy in certain instances, particularly for lighter models, thereby underscoring the sensitivity of architectures to background variations. This work provides a solid foundation for the future development of camera-based models, with a view to operational deployment across entire watersheds.

The second major contribution of the study lies in the implementation of a geometric model based on perspective projection to estimate the actual dimensions of objects detected from a 2D image. The model uses the camera's intrinsic and extrinsic parameters (focal length, sensor size, height, and installation angle) to reconstruct direction vectors and interpret the metric size of objects by intersection with a reference plane. Despite the simplifications inherent in the pinhole camera model (without optical correction), the results obtained after statistical correction achieve errors that approximate the image resolution limits (approximately 1.3 cm). This level of accuracy, adequate for estimation of mass or volume, confirms the robustness of the method when applied in real-world conditions.

CRediT authorship contribution statement

Gauthier Grimmer: Conceptualization, Methodology, Investigation, Software, Data curation, Writing - Original Draft, Writing - Review & Editing. Romain Wenger: Conceptualization, Methodology, Software, Formal analysis, Writing - Original Draft, Writing - Review & Editing, Validation, Funding acquisition, Supervision. Clément Flint: Methodology, Software, Writing - Original Draft, Writing - Review & Editing, Validation. Germain Forestier: Validation, Formal analysis, Writing - Review & Editing, Supervision. Gilles Rixhon: Validation, Writing - Review & Editing, Supervision. Valentin Chardon: Conceptualization, Formal analysis, Methodology, Writing - Original Draft, Writing - Review & Editing, Supervision, Validation, Funding acquisition, Project administration.

Declaration of competing interest

The authors declare that they have no known competing financial interests or personal relationships that could have appeared to influence the work reported in this paper.

Data availability

The dataset is available on demand by contacting the authors. The code is available on Github (Projective geometry: https://github.com/cflinto/projective-geo-sizing; deep learning models: https://github.com/g-grimmer/YOLO-WastDetect/; corresponding models weights: https://cloud.live.unistra.fr/index.php/s/MLQKkXPDaHWZH7D).

Acknowledgements

This research has been funded by the Zone Atelier Environnementale et Urbaine of Strasbourg.

We also would like to thank the University of Strasbourg through the Ecole Doctorale Sciences de la Terre et de l'Environnement (ED n° 413) for the PhD grant.

Thank you to David Eschbach and all the colleagues from the *Eurométropole* de *Strasbourg* for the support and the funding of the project.

We also thank Anne Puissant and Pierre-Alexis Herrault for their feedbacks. The authors would also like to acknowledge the High Performance Computing Center of the University of Strasbourg for supporting this work by providing scientific support and access to computing resources. Part of the computing resources were funded by the Equipex Equip@Meso project (Programme Investissements d'Avenir) and the CPER Alsacalcul/Big Data.

References

Aarnink, J., Beucler, T., Vuaridel, M., Ruiz-Villanueva, V., 2025. Automatic detection of floating instream large wood in videos using deep learning. Earth Surface Dynamics 13, 167–189.

Alabi, O.A., Ologbonjaye, K.I., Awosolu, O., Alalade, O.E., 2019. Public and environmental health effects of plastic wastes disposal: a review. J Toxicol Risk Assess 5, 1–13.

- Alif, M.A.R., Hussain, M., 2024. Yolov1 to yolov10: A comprehensive review of yolo variants and their application in the agricultural domain. arXiv preprint arXiv:2406.10139.
- Anowar, F., Sadaoui, S., Selim, B., 2021. Conceptual and empirical comparison of dimensionality reduction algorithms (pca, kpca, lda, mds, svd, lle, isomap, le, ica, t-sne). comput. sci. rev. 40, 100378 (2021).
- Apicella, A., Isgrò, F., Prevete, R., 2024. Don't push the button! exploring data leakage risks in machine learning and transfer learning. arXiv preprint arXiv:2401.13796.
- Armitage, S., Awty-Carroll, K., Clewley, D., Martinez-Vicente, V., 2022. Detection and classification of floating plastic litter using a vessel-mounted video camera and deep learning. Remote Sensing 14, 3425.
- Babu, M.A.A., Pandey, S.K., Durisic, D., Koppisetty, A.C., Staron, M., 2024. Improving image data leakage detection in automotive software. arXiv preprint arXiv:2410.23312.
- Birchfield, S., 1998. An introduction to projective geometry (for computer vision). Unpublished note, Stanford university 14.
- Bois, P., Staentzel, C., 2025. Rethinking our collective well-being by sliding from one to common health. BioScience, biaf013.
- Bouke, M.A., Abdullah, A., 2023. An empirical study of pattern leakage impact during data preprocessing on machine learning-based intrusion detection models reliability. Expert Systems with Applications 230, 120715.
- Bovcon, B., Muhovič, J., Vranac, D., Mozetič, D., Perš, J., Kristan, M., 2021. Mods—a usv-oriented object detection and obstacle segmentation benchmark. IEEE Transactions on Intelligent Transportation Systems 23, 13403–13418.
- Brown, C.F., Kazmierski, M.R., Pasquarella, V.J., Rucklidge, W.J., Samsikova, M., Zhang, C., Shelhamer, E., Lahera, E., Wiles, O., Ilyushchenko, S., et al., 2025. Alphaearth foundations: An embedding field model for accurate and efficient global mapping from sparse label data. arXiv preprint arXiv:2507.22291.

- Castro-Jiménez, J., González-Fernández, D., Fornier, M., Schmidt, N., Sempéré, R., 2019. Macro-litter in surface waters from the rhone river: Plastic pollution and loading to the nw mediterranean sea. Marine Pollution Bulletin 146, 60–66.
- Chang, Y.J., Wu, Y.D., Liao, Y.L., Wang, C.H., Wu, Y.C., 2024. Modified yolo network model for metaphase cell detection in antinuclear antibody images. Engineering Applications of Artificial Intelligence 127, 107392.
- Chardon, V., Grimmer, G., Wenger, R., 2025. A simple and low-cost method using active radio frequency identification to survey the mobility of plastic debris in rivers. Science of the Total Environment 999, 180336.
- De Vries, R., Egger, M., Mani, T., Lebreton, L., 2021. Quantifying floating plastic debris at sea using vessel-based optical data and artificial intelligence. Remote Sensing 13, 3401.
- Do Carmo, M.P., 2016. Differential geometry of curves and surfaces: revised and updated second edition. Courier Dover Publications.
- Donal, O., Kamarudin, L., Zakaria, A., Azmi, N., 2023. Automated detection of floating wood logs on river surfaces using yolov5 model for flood warning system, in: Journal of Physics: Conference Series, IOP Publishing. p. 012011.
- Figueiredo, R.B., Mendes, H.A., 2024. Analyzing information leakage on video object detection datasets by splitting images into clusters with high spatiotemporal correlation. IEEE Access.
- Gao, L., He, Y., Sun, X., Jia, X., Zhang, B., 2019. Incorporating negative sample training for ship detection based on deep learning. Sensors 19, 684.
- Ghiglione, J.F., Barbe, V., Bruzaud, S., Burgaud, G., Cachot, J., Eyheraguibel, B., Lartaud, F., Ludwig, W., Meistertzheim, A.L., Paul-Pont, I., et al., 2023. Mission tara microplastics: a holistic set of protocols and data resources for the field investigation of plastic pollution along the land-sea continuum in europe. Environmental Science and Pollution Research, 1–18.

- Ghosh, K., Bellinger, C., Corizzo, R., Branco, P., Krawczyk, B., Japkowicz, N., 2024. The class imbalance problem in deep learning. Machine Learning 113, 4845–4901.
- Girshick, R., Donahue, J., Darrell, T., Malik, J., 2014. Rich feature hierarchies for accurate object detection and semantic segmentation, in: Proceedings of the IEEE conference on computer vision and pattern recognition, pp. 580–587.
- Gómez, A.S., Scandolo, L., Eisemann, E., 2022. A learning approach for river debris detection. International Journal of Applied Earth Observation and Geoinformation 107, 102682.
- Gong, Y., Liu, G., Xue, Y., Li, R., Meng, L., 2023. A survey on dataset quality in machine learning. Information and Software Technology 162, 107268.
- González-Fernández, D., Cózar, A., Hanke, G., Viejo, J., Morales-Caselles, C., Bakiu, R., Barceló, D., Bessa, F., Bruge, A., Cabrera, M., et al., 2021. Floating macrolitter leaked from europe into the ocean. Nature Sustainability 4, 474–483.
- Gui, J., Chen, T., Zhang, J., Cao, Q., Sun, Z., Luo, H., Tao, D., 2024. A survey on self-supervised learning: Algorithms, applications, and future trends. IEEE Transactions on Pattern Analysis and Machine Intelligence
- Hanke, G., Galgani, F., Werner, S., Oosterbaan, L., Nilsson, P., Fleet, D.,
 Kinsey, S., Thompson, R., Van Franker, J.A., Vlachogianni, T., et al.,
 2013. Guidance on monitoring of marine litter in european seas. Centro
 Oceanográfico de Vigo .
- Hurley, R., Braaten, H.F.V., Nizzetto, L., Steindal, E.H., Lin, Y., Clayer, F., van Emmerik, T., Buenaventura, N.T., Eidsvoll, D.P., Økelsrud, A., et al., 2023. Measuring riverine macroplastic: Methods, harmonisation, and quality control. Water Research 235, 119902.
- Jaiswal, A., Babu, A.R., Zadeh, M.Z., Banerjee, D., Makedon, F., 2020. A survey on contrastive self-supervised learning. Technologies 9, 2.

- Jautzy, T., Herrault, P.A., Chardon, V., Schmitt, L., Rixhon, G., 2020. Measuring river planform changes from remotely sensed data—a monte carlo approach to assessing the impact of spatially variable error. Earth Surface Dynamics 8, 471–484.
- Jia, T., Kapelan, Z., de Vries, R., Vriend, P., Peereboom, E.C., Okkerman, I., Taormina, R., 2023. Deep learning for detecting macroplastic litter in water bodies: A review. Water Research 231, 119632.
- John, K., Saurette, D.D., Heung, B., 2025. The problematic case of data leakage: A case for leave-profile-out cross-validation in 3-dimensional digital soil mapping. Geoderma 455, 3.
- Johnson, J.M., Khoshgoftaar, T.M., 2019. Survey on deep learning with class imbalance. Journal of big data 6, 1–54.
- Kataoka, T., Yoshida, T., Yamamoto, N., 2024. Instance segmentation models for detecting floating macroplastic debris from river surface images. Frontiers in Earth Science 12, 1427132.
- Khanam, R., Hussain, M., 2024. Yolov11: An overview of the key architectural enhancements. arXiv preprint arXiv:2410.17725.
- Kumar, R., Manna, C., Padha, S., Verma, A., Sharma, P., Dhar, A., Ghosh, A., Bhattacharya, P., 2022. Micro (nano) plastics pollution and human health: How plastics can induce carcinogenesis to humans? Chemosphere 298, 134267.
- Kylili, K., Kyriakides, I., Artusi, A., Hadjistassou, C., 2019. Identifying floating plastic marine debris using a deep learning approach. Environmental Science and Pollution Research 26, 17091–17099.
- Landebrit, L., Sanchez, R., Soccalingame, L., Palazot, M., Kedzierski, M., Bruzeau, S., Albignac, M., Ludwig, W., Ghiglione, J.F., Ter Halle, A., 2024. Small microplastics have much higher mass concentrations than large microplastics at the surface of nine major european rivers. Environmental Science and Pollution Research, 1–16.
- Lebreton, L.C., Van Der Zwet, J., Damsteeg, J.W., Slat, B., Andrady, A., Reisser, J., 2017. River plastic emissions to the world's oceans. Nature communications 8, 15611.

- LeCun, Y., Bengio, Y., Hinton, G., 2015. Deep learning. Nature 521, 436–444.
- Lin, T.Y., Maire, M., Belongie, S., Hays, J., Perona, P., Ramanan, D., Dollár, P., Zitnick, C.L., 2014. Microsoft coco: Common objects in context, in: Computer vision–ECCV 2014: 13th European conference, zurich, Switzerland, September 6-12, 2014, proceedings, part v 13, Springer. pp. 740–755.
- Liro, M., Zielonka, A., van Emmerik, T.H., 2023. Macroplastic fragmentation in rivers. Environment International 180, 108186.
- Luo, W., Han, W., Fu, P., Wang, H., Zhao, Y., Liu, K., Liu, Y., Zhao, Z., Zhu, M., Xu, R., et al., 2022. A water surface contaminants monitoring method based on airborne depth reasoning. Processes 10, 131.
- Maharjan, N., Miyazaki, H., Pati, B.M., Dailey, M.N., Shrestha, S., Nakamura, T., 2022. Detection of river plastic using uav sensor data and deep learning. Remote Sensing 14, 3049.
- Mahmoud, H.F., 2019. Parametric versus semi and nonparametric regression models. arXiv preprint arXiv:1906.10221.
- Malagon-Borja, L., Fuentes, O., 2009. Object detection using image reconstruction with pca. Image and Vision Computing 27, 2–9.
- Masko, D., Hensman, P., 2015. The impact of imbalanced training data for convolutional neural networks.
- Mohr, R., Triggs, B., 1996. Projective geometry for image analysis, in: XVI-IIth International Symposium on Photogrammetry & Remote Sensing (IS-PRS'96).
- Moulavi, D., Jaskowiak, P.A., Campello, R.J., Zimek, A., Sander, J., 2014. Density-based clustering validation, in: Proceedings of the 2014 SIAM international conference on data mining, SIAM. pp. 839–847.
- Munappy, A.R., Bosch, J., Olsson, H.H., Arpteg, A., Brinne, B., 2022. Data management for production quality deep learning models: Challenges and solutions. Journal of Systems and Software 191, 111359.

- Neves, D., Sobral, P., Ferreira, J.L., Pereira, T., 2015. Ingestion of microplastics by commercial fish off the portuguese coast. Marine pollution bulletin 101, 119–126.
- Nunkhaw, M., Miyamoto, H., 2024. An image analysis of river-floating waste materials by using deep learning techniques. Water 16, 1373.
- Oliveira, F.H.M., Machado, A.R., Andrade, A.O., 2018. On the use of t-distributed stochastic neighbor embedding for data visualization and classification of individuals with parkinson's disease. Computational and mathematical methods in medicine 2018, 8019232.
- Palmas, F., Cau, A., Podda, C., Musu, A., Serra, M., Pusceddu, A., Sabatini, A., 2022. Rivers of waste: Anthropogenic litter in intermittent sardinian rivers, italy (central mediterranean). Environmental Pollution 302, 119073.
- Prata, J.C., da Costa, J.P., Lopes, I., Andrady, A.L., Duarte, A.C., Rocha-Santos, T., 2021. A one health perspective of the impacts of microplastics on animal, human and environmental health. Science of the Total Environment 777, 146094.
- Pulgar, F.J., Rivera, A.J., Charte, F., del Jesus, M.J., 2017. On the impact of imbalanced data in convolutional neural networks performance, in: Hybrid Artificial Intelligent Systems: 12th International Conference, HAIS 2017, La Rioja, Spain, June 21-23, 2017, Proceedings 12, Springer. pp. 220-232.
- Rech, S., Macaya-Caquilpán, V., Pantoja, J., Rivadeneira, M., Madariaga, D.J., Thiel, M., 2014. Rivers as a source of marine litter—a study from the se pacific. Marine pollution bulletin 82, 66–75.
- Redmon, J., Divvala, S., Girshick, R., Farhadi, A., 2016. You only look once: Unified, real-time object detection, in: Proceedings of the IEEE conference on computer vision and pattern recognition, pp. 779–788.
- Réserves Naturelles de 2023. France, Réserve naturelle nationale du massif forestier de la robertsau de wantzenau. URL: https://reserves-naturelles.org/reserves/ massif-forestier-de-la-robertsau-et-de-la-wantzenau. accessed April 2025.

- Sasse, L., Nicolaisen-Sobesky, E., Dukart, J., Eickhoff, S., Götz, M., Hamdan, S., Komeyer, V., Kulkarni, A., Lahnakoski, J., Love, B., et al., 2025. Overview of leakage scenarios in supervised machine learning. Journal of Big Data 12, 1–23.
- Schöneich-Argent, R.I., Dau, K., Freund, H., 2020. Wasting the north sea?—a field-based assessment of anthropogenic macrolitter loads and emission rates of three german tributaries. Environmental Pollution 263, 114367.
- Schwindt, S., Meisinger, L., Negreiros, B., Schneider, T., Nowak, W., 2024. Transfer learning achieves high recall for object classification in fluvial environments with limited data. Geomorphology 455, 109185.
- Seide, F., Li, G., Chen, X., Yu, D., 2011. Feature engineering in context-dependent deep neural networks for conversational speech transcription, in: 2011 IEEE Workshop on Automatic Speech Recognition & Understanding, IEEE. pp. 24–29.
- Siméoni, O., Vo, H.V., Seitzer, M., Baldassarre, F., Oquab, M., Jose, C., Khalidov, V., Szafraniec, M., Yi, S., Ramamonjisoa, M., et al., 2025. Dinov3. arXiv preprint arXiv:2508.10104.
- Skalska, K., Ockelford, A., Ebdon, J.E., Cundy, A.B., 2020. Riverine microplastics: Behaviour, spatio-temporal variability, and recommendations for standardised sampling and monitoring. Journal of Water Process Engineering 38, 101600.
- Suteja, Y., Parwati, E., Budhiman, S., Radjawane, I.M., Hartuti, M., Afgatiani, P.M., Ulfa, A., Dewi, E.K., Purwiyanto, A.I.S., et al., 2025. Spatial patterns and types of marine anthropogenic debris on touristic beaches along the eastern indian ocean: A preliminary study from southern sumatera island, indonesia. Regional Studies in Marine Science 81, 103970.
- Tampu, I.E., Eklund, A., Haj-Hosseini, N., 2022. Inflation of test accuracy due to data leakage in deep learning-based classification of oct images. Scientific Data 9, 580.
- Tao, H., Zheng, Y., Wang, Y., Qiu, J., Stojanovic, V., 2024. Enhanced feature extraction yolo industrial small object detection algorithm based on receptive-field attention and multi-scale features. Measurement Science and Technology 35, 105023.

- Tata, G., Royer, S.J., Poirion, O., Lowe, J., 2021. A robotic approach towards quantifying epipelagic bound plastic using deep visual models. arXiv preprint arXiv:2105.01882.
- Tramoy, R., Gasperi, J., Dris, R., Colasse, L., Fisson, C., Sananes, S., Rocher, V., Tassin, B., 2019. Assessment of the plastic inputs from the seine basin to the sea using statistical and field approaches. Frontiers in Marine Science 6, 151.
- Tzutalin, 2015. LabelImg [computer software]. https://github.com/tzutalin/labelImg. GitHub repository.
- Ultralytics, 2024. Tasks oriented object detection (obb). https://docs.ultralytics.com/fr/tasks/obb/. Accessed on June 23, 2025.
- Ultralytics Inc., 2019. Model training with ultralytics yolo. https://docs.ultralytics.com/modes/train/. Accessed April 11, 2019.
- Van Emmerik, T., Schwarz, A., 2020. Plastic debris in rivers. Wiley Interdisciplinary Reviews: Water 7, e1398.
- Van Lieshout, C., van Oeveren, K., van Emmerik, T., Postma, E., 2020. Automated river plastic monitoring using deep learning and cameras. Earth and space science 7, e2019EA000960.
- Wang, J., Zhao, H., 2024. Improved yolov8 algorithm for water surface object detection. Sensors 24, 5059.
- Waring, R.H., Harris, R., Mitchell, S., 2018. Plastic contamination of the food chain: A threat to human health? Maturitas 115, 64–68.
- Wegmann, M., Zipperling, D., Hillenbrand, J., Fleischer, J., 2021. A review of systematic selection of clustering algorithms and their evaluation. arXiv preprint arXiv:2106.12792.
- Yalçın, S., Ekenel, H.K., 2024. Impact of surface reflections in maritime obstacle detection. arXiv preprint arXiv:2410.08713.
- Ye, J., Zhang, Y., Li, P., Guo, Z., Zeng, S., Wei, T., 2025. Real-time dense small object detection model for floating litter detection and removal on water surfaces. Marine Pollution Bulletin 218, 118189.

- Ying, X., 2019. An overview of overfitting and its solutions, in: Journal of physics: Conference series, IOP Publishing. p. 022022.
- Zhang, X., Min, C., Luo, J., Li, Z., 2023. Yolov5-ff: detecting floating objects on the surface of fresh water environments. Applied Sciences 13, 7367.

Appendix A

Plane from a point and two non-colinear vectors. In three-dimensional space, a plane can be defined by a unit normal vector \vec{n} and a scalar offset d, such that every point \vec{x} on the plane satisfies the equation:

$$\vec{n} \cdot \vec{x} + d = 0. \tag{19}$$

This is known as the *implicit form* of a plane equation (Do Carmo, 2016).

To construct such a plane from geometric data, consider a known point $\vec{P}_0 \in \mathbb{R}^3$ that lies on the plane, along with two non-colinear vectors \vec{v}_1 and \vec{v}_2 that span the plane.

We compute the normal vector \vec{n} as the normalized cross product of these vectors:

$$\vec{n} = \text{normalize}(\vec{v}_1 \times \vec{v}_2).$$
 (20)

Then, the offset d is determined so that the plane passes through \vec{P}_0 , yielding:

$$d = -\vec{n} \cdot \vec{P}_0. \tag{21}$$

Intersection of a ray with a plane. A ray in 3D space is defined by an origin point $\vec{o} \in \mathbb{R}^3$ and a direction vector $\vec{v} \in \mathbb{R}^3$, and is parameterized as:

$$\vec{r}(t) = \vec{o} + t\vec{v} \quad \text{for } t \ge 0. \tag{22}$$

The ray extends from \vec{o} in the direction of \vec{v} , and the parameter t controls the distance traveled along the ray.

To compute the intersection point \vec{p} between the ray and the plane, we substitute the ray equation into the plane equation:

$$\vec{n} \cdot (\vec{o} + t_{intersection}\vec{v}) + d = 0.$$
 (23)

Solving for t gives:

$$t_{intersection} = -\frac{\vec{n} \cdot \vec{o} + d}{\vec{n} \cdot \vec{v}}$$
 provided that $\vec{n} \cdot \vec{v} \neq 0$. (24)

If the resulting $t_{intersection} \geq 0$, the intersection lies in the forward direction of the ray and is considered valid. The corresponding 3D intersection point is then:

$$\vec{p} = \vec{o} + t_{intersection} \vec{v}. \tag{25}$$

Distance from a point to a plane. Given a plane $\vec{n} \cdot \vec{x} + d = 0$ and a point $\vec{p} \in \mathbb{R}^3$, the signed distance from the point to the plane is:

$$distance = \vec{n} \cdot \vec{p} + d. \tag{26}$$

The geometric (unsigned) distance is given by:

$$distance = |\vec{n} \cdot \vec{p} + d|, \qquad (27)$$

which corresponds to the shortest distance between the point and any location on the plane.